

# Finding emergence in data: causal emergence inspired dynamics learning

Mingzhe Yang<sup>1</sup>, Zhipeng Wang<sup>1</sup>, Kaiwei Liu<sup>1</sup>, Yingqi Rong<sup>2,3</sup>, Bing Yuan<sup>2</sup>, Jiang Zhang<sup>1,2\*</sup>

<sup>1</sup> School of Systems Science, Beijing Normal University, 100875, Beijing, China

<sup>2</sup>Swarma Research, 102300, Beijing, China

<sup>3</sup>Johns Hopkins University, 21218, Laurel, MD, USA

## Abstract

Modelling complex dynamical systems in a data-driven manner is challenging due to the presence of emergent behaviors and properties that cannot be directly captured by micro-level observational data. Therefore, it is crucial to develop a model that can effectively capture emergent dynamics at the macro-level and quantify emergence based on the available data. Drawing inspiration from the theory of causal emergence, this paper introduces a machine learning framework aimed at learning macro-dynamics within an emergent latent space. The framework achieves this by maximizing the effective information (EI) to obtain a macro-dynamics model with stronger causal effects. Experimental results on both simulated and real data demonstrate the effectiveness of the proposed framework. Not only does it successfully capture emergent patterns, but it also learns the coarse-graining strategy and quantifies the degree of causal emergence in the data. Furthermore, experiments conducted on environments different from the training dataset highlight the superior generalization ability of our model.

**Keywords:**causal emergence; dynamics learning; effective information; coarse-graining; invertible neural network

## 1. Main

The climate system, ecosystems, bird flocks, ant colonies, cells, brains, and many other complex systems are composed of numerous interacting elements and exhibit a wide range of nonlinear dynamical behaviors[1, 2]. In the past few decades, the research topic of data-driven modeling complex systems has gained significant attention, driven by the increasing availability and accumulation of data from real dynamical systems[3, 4, 5, 6]. However, complex systems always exhibit emergent behaviors [7, 1]. That means some interesting emergent patterns or dynamical behaviors such as waves[8], periodic oscillations[9] and solitons[10] can hardly be directly observed and identified from the micro-level behavioral data. Therefore, the identification and measure of emergence and the capture of emergent dynamical patterns solely from observational raw data have become crucial challenges in complex systems research that extend beyond data-driven modeling[11, 12, 13, 14]. But in order to address these problems, it is necessary to first develop a quantitative understanding of emergence.

Emergence, as a distinctive feature of complex systems [7], has historically been challenging to quantify and describe in quantitative terms[15, 16]. However, the concept of causal emergence, proposed by Erik Hoel, provides a framework to address this difficulty [17, 18]. Hoel's theory aims to understand emergence through the lens of causality. The connection between emergence and causality is implied in the descriptive definition of emergence, as stated in the work by J. Fromm[19]. According to this definition, a macro-level property, such as patterns or dynamical behaviors, is considered emergent if it cannot be explained or directly attributed to the individuals in the system. The theory of causal emergence formalizes this concept within the framework of discrete Markov dynamical systems. As shown in Figure 1(a), Hoel et al's theory states that if a system exhibits stronger causal effects after a specific coarse-graining transformation compared to the original system, then causal emergence has occurred. In Hoel's framework, the degree of causal effect in a dynamical system is quantified using effective information (EI) [20]. EI, which is denoted as  $\mathcal{J}$  in this paper, can be

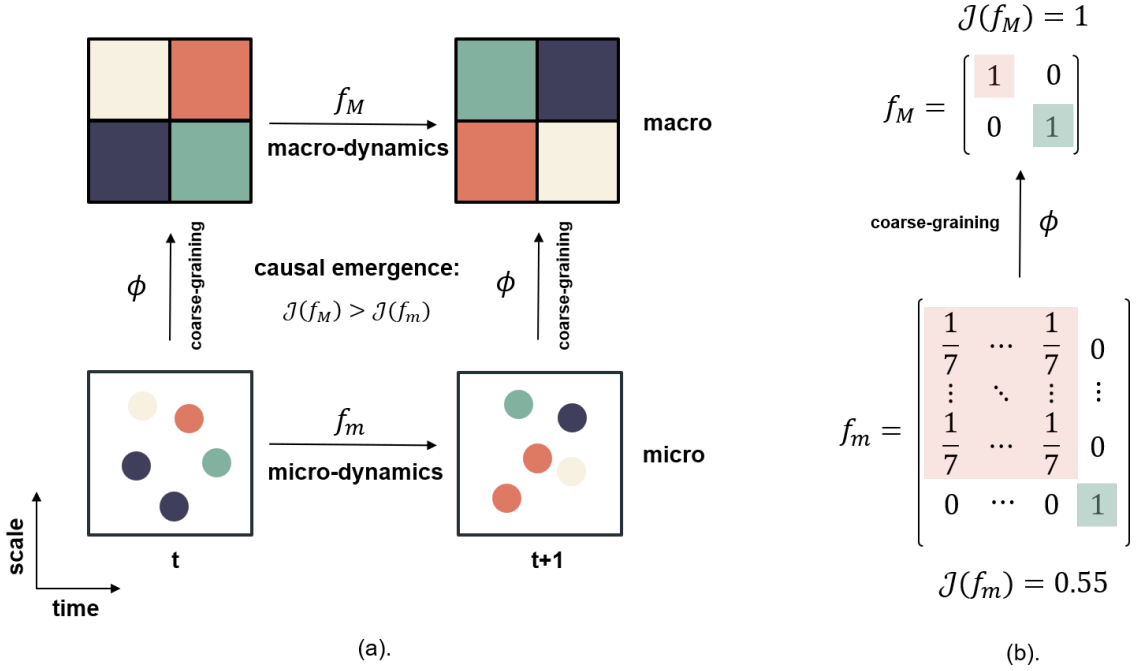


**Figure 1.** (a) An illustration of the fundamental concept of Erik Hoel’s theory of causal emergence. (b) A case demonstrating causal emergence in a discrete Markov system. The micro-dynamics consist of eight micro-states. During the coarse-graining process, the first seven states are grouped together as one macro-state, while the eighth micro-state corresponds to the second macro-state. As a result, a transition probability matrix is formed at the macro-scale, where the effective information  $\mathcal{J}(f_M) = 1$  (calculated using Equation 8), which is greater than  $\mathcal{J}(f_m) = 0.55$ . This difference,  $\Delta\mathcal{J} = 0.45$ , indicates the occurrence of causal emergence, as  $\Delta\mathcal{J} > 0$ .

understood as an intervention-based version of mutual information between two successive states in a dynamical system over time. It is a measure that solely depends on the system’s dynamics. If a dynamical system is more deterministic and non-degenerate, meaning that the temporal adjacent states can be inferred from each other in both directions of the time arrow, then it will have a larger EI [17]. This measure has been shown to be compatible with other well-known measures of causal effect[21]. Figure 1(b) gives an example of causal emergence for simple Markov chain.

While causal emergence theory has successfully quantified emergence using effective information (EI) and has found applications in various fields[22, 23, 24], it does not directly address the problem of finding causal emergence in data[11, 12]. In other words, it does not provide a method to determine whether causal emergence has occurred within a system and in what degree based solely on observational data of its behavior. The reason is, in Hoel’s framework, an appropriate coarse-graining method needs to be specified. However, in many cases, we do not have prior knowledge of how to coarse-grain a dynamical system. Therefore, all elements, including the coarse-graining strategy, macro- and micro-level dynamics, need to be learned from the data itself[12]. Indeed, once the learning process is completed, we can compare the strength of causal effects (measured by EI) in dynamics at different scales to identify causal emergence from the data. Therefore, the problem of finding causal emergence within Hoel’s theoretical framework is equivalent to the problem of data-driven modeling within a coarse-grained space for complex systems. Building models for complex systems at multiple coarse-grained levels within learned emergent spaces is of paramount importance for both finding causal emergence and data-driven modeling in complex systems.

Recently, several machine learning frameworks have been proposed to learn and simulate the dynamics of complex systems in coarse-grained latent or hidden spaces. For example, the work by Pantelis R. Vlachas et al. utilizes autoencoders to learn coarse-grained representations of raw data, and also employs recurrent neural networks to capture the effective dynamics within the latent space[25]. This framework is applicable to systems ranging from

chemistry to fluid mechanics and reduces the computational effort. F.P. Kemeth and T. Bertalan et. al. have developed a data-driven method to learn partial differential equations (PDEs) within a learned latent space[14]. By combining the theory of manifolds with the representational capacity of neural networks, D. Floryan and M.D. Graham develop a method to learn intrinsic state variables directly from time-series data, as well as predictive models for their dynamics[26]. Other works, e.g. [27, 28], even tried to build effective dynamical models on several coarse-grained scales. By combining the techniques of dynamics learning on the latent space with reinforcement learning, world model-based reinforcement learning algorithms have achieved state-of-the-art performance on various tasks[29, 30].

Indeed, while these present works focus on learning effective or latent dynamics for improving predictions, they may not directly address the essence of causal emergence, which involves stronger causality. According to Judea Pearl’s hierarchy of causality, prediction-based learning is situated at the level of association and cannot address the challenges related to intervention and counterfactuals[31]. Empirically, dynamics learned solely based on predictions may be influenced by the distributions of the input data, which can be limited by data diversity and the problem of over fitting models[32]. However, what we truly desire is an invariant causal mechanism or dynamics that are independent of the input data. This allows the learned mechanism or dynamics to be adaptable to broader domains, generalizable to areas beyond the distribution of training data, and capable of accommodating diverse interventions[33, 34]. Unfortunately, few studies have explored the integration of causality and latent space dynamics to address the challenges of data-driven modeling in complex systems.

Inspired by the theory of causal emergence, this paper aims to address the challenge of learning causal mechanisms within a learned coarse-grained macro-level(latent) space. The approach involves maximizing the EI of the emergent macro-level dynamics, which is equivalent to maximizing the degree of causal effect in the learned coarse-grained dynamics. By artificially intervening the distributions of input data as uniform distribution, this maximization process helps separating the invariant causal mechanisms from the variant data distribution as much as possible. To achieve this, a novel machine learning framework called Neural Information Squeezer Plus (NIS+) is proposed. NIS+ extends the previous framework (NIS) and combines invertible neural networks with several other techniques to maximize EI under coarse-grained representations. As shown in Figure 2, NIS+ not only learns emergent macro-dynamics and coarse-grained strategies but also captures emergent patterns and quantifies the degree of causal emergence from time series data. Mathematical theorems ensure the flexibility of our framework in different application scenarios, such as cellular automata and multi-agent systems. Numerical experiments demonstrate the effectiveness of NIS+ in capturing emergent behaviors and finding causal emergence in various simulations, including SIR dynamics[35], bird flocking (Boids model)[36], and the Game of Life[37]. Additionally, NIS+ is applied to find emergent features in real brain data from 830 subjects while watching the same movie. Experiments also demonstrate that the learned dynamical model exhibits improved performance in terms of out-of-distribution generalization compared to other models.

## 2. Finding causal emergence in data

Finding causal emergence in time series data involves two sub-problems: **emergent dynamics learning** and **causal emergence quantification**. In the first problem, both the dynamics in micro- and macro-level and the coarse-graining strategy should be learned from data. After that, we can measure the degree of causal emergence and judge if emergence occurs in data according to the learned micro- and macro-dynamics.

### 2.1. Problem definition

Suppose the behavioral data of a complex dynamical system is a time series  $\{\mathbf{x}_t\}$  with time steps  $t = 1, 2, \dots, T$  and dimension  $p$ , they form observable micro-states. And we assume that there are no unobserved variables. The problem of **emergent dynamics learning** is to find three functions according to the data: a coarse-graining strategy  $\phi : \mathcal{R}^p \rightarrow \mathcal{R}^q$ , where  $q \leq p$  is the dimension of macro-states which is given as a hyper-parameter, a corresponding anti-coarsening strategy  $\phi^\dagger : \mathcal{R}^p \rightarrow \mathcal{R}^q$ , and a macro-dynamics  $f_q$ , such that the EI of macro-dynamics  $f_q$  is maximized under the constraint that the predicted  $\hat{\mathbf{x}}_{t+1}$  by  $\phi$ ,  $f_q$ , and  $\phi^\dagger$  is closed to the real data of  $\mathbf{x}_{t+1}$ :

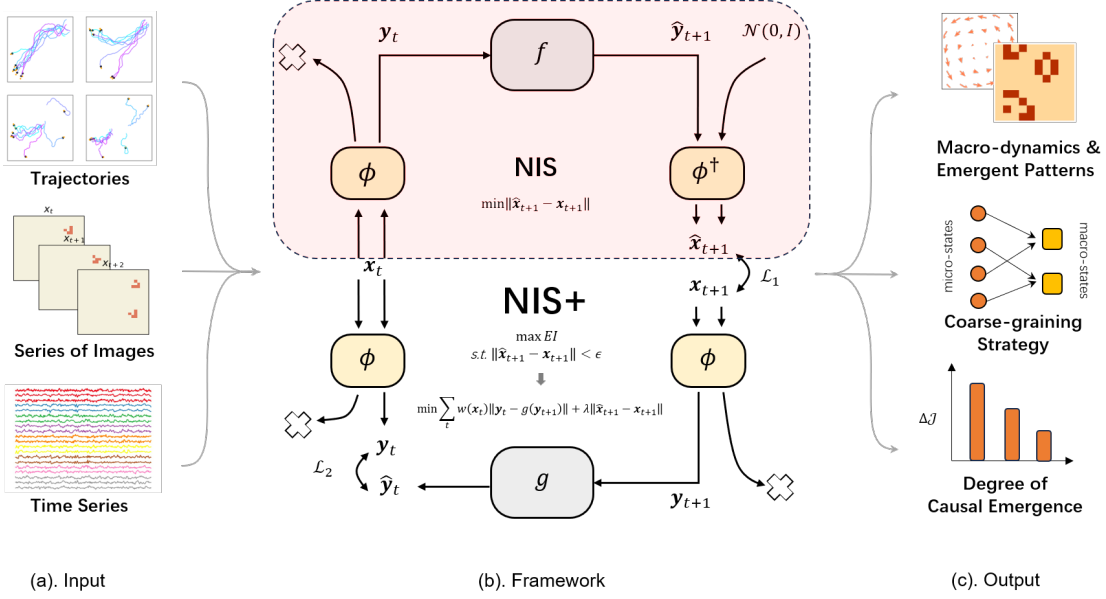


**Figure 2.** The workflow and architecture of our proposed framework, Neural Information Squeezer Plus (NIS+), for discovering causal emergence within data. (a) Various forms of input data from our studied simulation systems such as the Boid flocking model (multi-agent system), Conway’s Game of Life (two-dimensional cellular automata), and real brain fMRI time series data. (b) The framework of our proposed model, NIS+, which incorporates our previous model, NIS. The boxes represent functions or neural networks, and the arrow pointing to a cross represents the operation of information discarding.  $x_t$  and  $x_{t+1}$  represent the observational data of micro-states, while  $\hat{x}_{t+1}$  represents the predicted micro-state.  $y_t = \phi(x_t)$  and  $y_{t+1} = \phi(x_{t+1})$  represent the macro-states obtained by encoding the micro-states using the encoder.  $\hat{y}_t = \phi(\hat{x}_t)$  and  $\hat{y}_{t+1} = \phi(\hat{x}_{t+1})$  represent the predicted macro-states obtained by encoding the predictions of micro-states. The mathematical problems that each framework aims to solve are also illustrated in the figure. (c) The various output forms of NIS+, which include the learned macro-dynamics, captured emergent patterns, functions of coarse-graining, and the degree of causal emergence.

$$\begin{aligned} & \max_{\phi, f_q, \phi^\dagger} \mathcal{J}(f_q), \\ & \text{s.t. } \begin{cases} \|\hat{x}_{t+1} - x_{t+1}\| < \epsilon, \\ \hat{x}_{t+1} = \phi^\dagger(f_q(\phi(x_t))). \end{cases} \end{aligned} \quad (1)$$

Where,  $\mathcal{J}$  is the appropriate version of EI to be maximized. For continuous dynamical systems that mainly considered in this paper,  $\mathcal{J}$  is the dimension averaged effective information (dEI)[12](see method section 5.3),  $\epsilon$  is a given small constant.

The objective of maximizing EI in Equation 1 is to enhance the causal effect of the macro-dynamics  $f_q$ . However, directly maximizing EI, as illustrated in Figure 1, can lead to trivial solutions, as pointed out by Zhang et al. [12]. To address this issue, constraints are introduced to prevent such problems. The constraints in Equation 1 ensure that the macro-dynamics  $f_q$  can simulate the micro-dynamics in the data as accurately as possible, with the prediction error being less than a given threshold  $\epsilon$ .

This is achieved by mapping the micro-state  $x_t$  to the macro-state  $y_t = \phi(x_t)$  at each time step. The macro-dynamics  $f_q$  then makes a one-step prediction to obtain  $\hat{y}_{t+1} = f_q(\phi(x_t))$ . Subsequently, an anti-coarsening strategy  $\phi^\dagger$  is employed to decode  $\hat{y}_{t+1}$  back into the micro-state, resulting in the reconstructed micro-state  $\hat{x}_{t+1} = \phi^\dagger(\hat{y}_{t+1})$ . The entire computational process can be visualized by referring to the upper part(NIS) in Figure 2b.

By changing  $q$  we can obtain macro-dynamics in various dimensions. If  $q = p$ , then  $f_p$  becomes the learnt micro-dynamics. Then we can compare  $\mathcal{J}_q$  and  $\mathcal{J}_p$  for any  $q$ . The problem of **causal emergence quantification** can be defined as the calculation of the following difference,

$$\Delta\mathcal{J} \equiv \mathcal{J}(f_q) - \mathcal{J}(f_p), \quad (2)$$

where  $\Delta\mathcal{J}$  is defined as the degree of causal emergence. The micro-dynamics  $f_p$  is also obtained by solving Equation 1 with dimension  $q = p$ . If  $\Delta\mathcal{J} > 0$ , then we say causal emergence occurs within the data. For how to compute the EI of a neural network numerically, please refer to method section 5.3.

## 2.2. Solution

While, solving the optimization problem defined in Equation 1 directly is difficult because the objective function  $\mathcal{J}$  is the mutual information after intervention which deserved special process.

To tackle this problem, we convert the problem defined in Equation 1 into a new optimization problem without constraints, that is:

$$\min_{f, g, \phi, \phi^\dagger} \sum_{t=1}^{T-1} w(\mathbf{x}_t) \|\mathbf{y}_t - g(\mathbf{y}_{t+1})\| + \lambda \|\hat{\mathbf{x}}_{t+1} - \mathbf{x}_{t+1}\|, \quad (3)$$

where  $\hat{\mathbf{x}}_{t+1} = \phi^\dagger(f(\phi(\mathbf{x}_t)))$ .  $\mathbf{y}_t = \phi(\mathbf{x}_t)$  and  $\mathbf{y}_{t+1} = \phi(\mathbf{x}_{t+1})$  are the macro-states.  $g: \mathcal{R}^q \rightarrow \mathcal{R}^q$  is a new function that we introduce to simulate the inverse macro-dynamics on the macro-state space, that is to map each macro-state at  $t+1$  time step back to the macro-state at  $t$  time step.  $\lambda$  is a Lagrangian multiplier which will be taken as a hyper-parameter in experiments.  $w(\mathbf{x}_t)$  is the inverse probability weights which is defined as:

$$w(\mathbf{x}_t) = \frac{\tilde{p}(\mathbf{y}_t)}{p(\mathbf{y}_t)} = \frac{\tilde{p}(\phi(\mathbf{x}_t))}{p(\phi(\mathbf{x}_t))}, \quad (4)$$

where  $\tilde{p}$  is the new distribution of macro-states  $\mathbf{y}_t$  after intervention for  $do(\mathbf{y}_t \sim U_q)$ , and  $p$  is the natural distribution of the data. In practice,  $p(\mathbf{y}_t)$  is estimated through kernel density estimation (KDE)[38](see method section 5.4). The approximated distribution,  $\tilde{p}(\mathbf{y}_t)$ , is assumed to be a uniform distribution, which is characterized by a constant value. Consequently, the weight  $w$  is computed as the ratio of these two distributions. Mathematical theorems mentioned in method section and proved in Support Information 7.2.1 guarantee this new optimization problem (Equation 3) is equivalent to the original one (Equation 1).

In Equation 3, each term in the objective function consists of two components: the error of micro-dynamics reconstruction (denoted as  $\mathcal{L}_1$ ) and the error of inverse macro-dynamics simulation (denoted as  $\mathcal{L}_2$ ). The prediction of micro-states is achieved by decoding the predicted macro-states into micro-states. We aim to estimate the forward and inverse dynamics within the learned macro-state space by fitting the data. As a result, the complex functional optimization problem is transformed into a standard machine learning problem.

We introduce a novel neural network called Neural Information Squeezer Plus (NIS+) to parameterize all the functions  $\phi, \phi^\dagger, f, g$ , as illustrated in Figure 2b. The architecture consists of two parts: the upper part aims to minimize  $\mathcal{L}_1$ , while the lower part aims to minimize  $\mathcal{L}_2$ . Notably, the upper part shares the same structure as the Neural Information Squeezer (NIS), which was proposed in our previous work [12].

NIS simplifies the coarse-graining strategy by employing an encoder  $\phi$ , which is modeled by an invertible neural network followed by a projection operation, as depicted in the upper part of Figure 2. Consequently, the de-coarsening function  $\phi^\dagger$  can be obtained by reversing the process and passing the macro-state back through the same invertible neural network. Any missing dimensions can be filled in with Gaussian noise. The macro-dynamics are learned using a feed-forward neural network  $f$ . For more details, please refer to the method section and the Support Information in Section 7.7.

When applying NIS or NIS+ to data generated by various complex systems, such as cellular automata and multi-agent systems, the architecture of the encoder and decoder needs to be extended to accommodate stacked or parallel structures. Fortunately, these architectures are highly adaptable to different real-world scenarios, allowing for the retention of important properties. Mathematical theorems ensure that the maximization of EI can be achieved through these extended frameworks. For more details, please refer to the method section and the Support Information 7.2.2.

### 3. Results

We will validate the effectiveness of the NIS+ framework through several numerical experiments in which data is generated by different artificial models including dynamical systems, multi-agents systems, and cellular automata. After that, we also apply NIS+ to real fMRI data of human subjects to find interesting macro-level variables and dynamics.

#### 3.1. SIR

The design of the first experiment involves a simple dynamical system: the SIR(susceptible, infected, and recovered or died) model. Its purpose is to test our model’s ability to remove noise, uncover effective macroscopic dynamics, and demonstrate generalization beyond the training dataset distribution. Additionally, we compare our model with other different models. To test the model’s ability to uncover real macroscopic dynamics through maximizing EI, we first design the dynamical equations (SIR) that the macro-state should satisfy as a ground truth comparison. Next, we introduce noise to generate micro-state data. In this way, the learning algorithms was required to recover the effective macroscopic dynamics from these noisy data. Formally, the macro-dynamics is described as follows:

$$\begin{cases} \frac{dS}{dt} = -\beta SI, \\ \frac{dI}{dt} = \beta SI - \gamma I, \\ \frac{dR}{dt} = \gamma I, \end{cases} \quad (5)$$

where  $S, I, R \in [0, 1]$  represents the proportions of healthy, infected and recovered or died individuals in a population,  $\beta = 1$  and  $\gamma = 0.5$  represent infection and recovery or death rates for an infected individual, respectively. As  $S, I$ , and  $R$  satisfy  $S + I + R = 1$ , only  $(S, I)$  are used to form the macro-state variable  $\mathbf{y} = (S, I)$ , and  $R$  is removed. Figure 3(a) shows the phase space of the SIR dynamics. Because the model has only two degrees of freedom, all macro-states are distributed on a triangular plane in three dimensions.

We then introduce Gaussian noises and expand  $\mathbf{y}$  into a four-dimensional vector to form a microscopic state:

$$\begin{cases} \mathbf{S}' = (S, S) + \boldsymbol{\xi}_1, \\ \mathbf{I}' = (I, I) + \boldsymbol{\xi}_2. \end{cases} \quad (6)$$

Among which,  $\boldsymbol{\xi}_1, \boldsymbol{\xi}_2 \sim N(0, \Sigma)$  are two-dimensional Gaussian noises and independent each other, and  $\Sigma$  is the correlation matrix. When the off-diagonal elements of  $\Sigma$  are non-zero, the dimensions of micro-states are correlated. In this way, we obtain a micro-states sequence  $\mathbf{x}_t = (\mathbf{S}', \mathbf{I}')$  as the training samples in the experiment. We expect the algorithms are able to remove the noises and capture the real SIR dynamics model at the macro level.

To compare the capabilities of NIS+ on recovering macro-dynamics with NIS and feed-forward neural network with the same amount of parameters as benchmark models, we train all the compared models on the same dataset and require them to predict future states with multiple time steps(10 steps) on test dataset. As shown in Figure 3(c), the result show that NIS+(green bars) outperforms other competitors on multi-step prediction. Figure 3(b) shows the evolution of EI (dimension averaged)  $\mathcal{J}$  as training epochs, we can clearly observe that the curves of NIS+(red) increase faster than comparison models which means NIS+ can maximize  $\mathcal{J}$  with higher efficiency. We further compare the normalized vector fields of the real SIR dynamics  $d\mathbf{x}_t/dt$  and the learnt emergent dynamics as shown in Figure 3(d). The learned vector field(green arrows) can be approximately regarded as a 180-degree rotation of the ground truth(red arrows) especially in the central region. That means, the learnt emergent dynamics and the real SIR dynamics have a one to one correspondence.

To assess the model’s generalization ability beyond the training dataset, in addition to the regular training and testing, we also conduct experiments where the model was trained on a subset of the data and tested on the complete dataset. The training samples in this experiment are shown in the dotted area in Figure 3(a)(the area with  $S \leq \frac{1}{3}$  is missing), and the test samples are also in the blue triangle. As shown in Figure 3(c), the performance of out-of-distribution generalization of NIS+ are better than other benchmarks although the test region is beyond the trained region. And the differences among different models are larger on partial dataset.

Therefore, these experiments manifest that by maximizing EI and learning an independent causal mechanism, NIS+ can effectively disregard noise within the data and accurately learn the ground truth macro-dynamics. Additionally, NIS+ demonstrates superior performance in



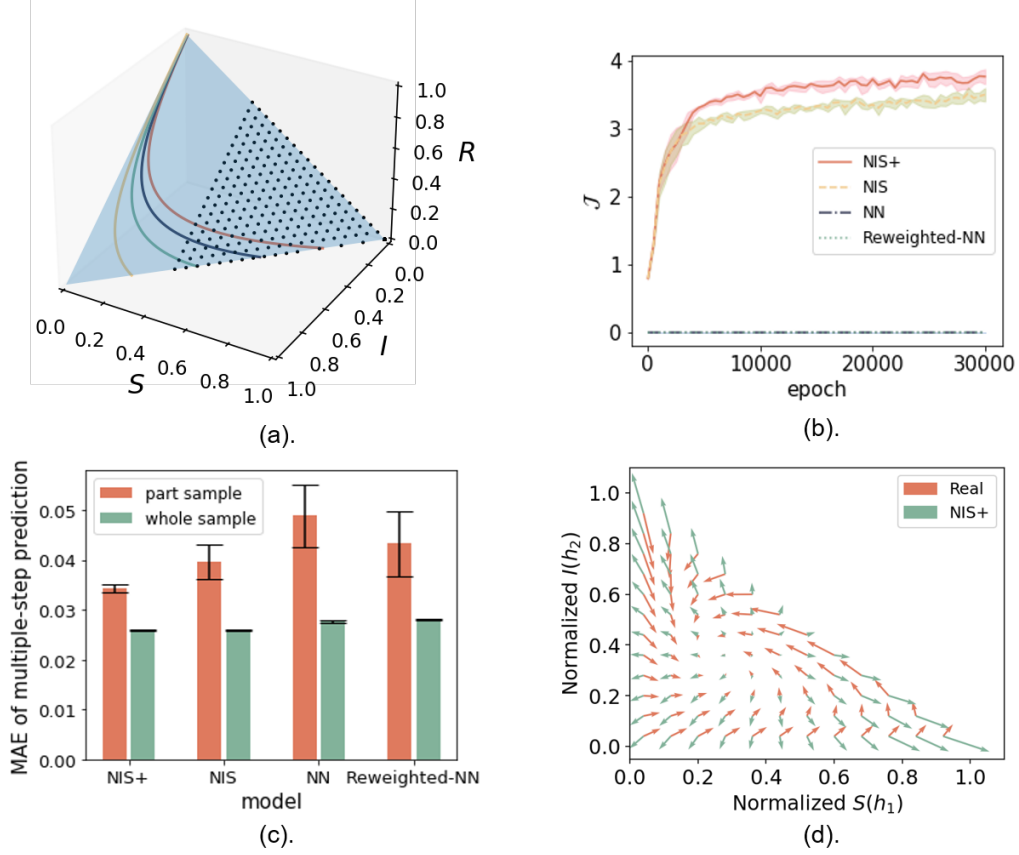


**Figure 3.** The experimental results of the SIR model with observational noise. (a) The phase space of the SIR model, along with four example trajectories with the same infection and recovery or death rates. The full dataset (blue area) and the partial dataset (dotted area) used for training are also displayed, consisting of 63,000 and 42,000 uniformly distributed data points, respectively. (b) The curves depict the change in dimension-averaged effective information ( $\mathcal{J}$ ) with training epochs for different models. These models include a feed-forward neural network (NN), a feed-forward neural network with inverse probability weighting technique (Reweighted-NN), NIS, and NIS+. The lines represent the means, while the band widths represent the standard deviations of five repeated experiments. For NIS+, two stages are separated at the 3000th epoch (see Method section 5.2.4). In the second stage (after 3000 epochs), NIS+ incorporates inverse probability weighting and bidirectional dynamic learning, distinguishing it from the NIS model. Reweighted-NN and NN have the same number of parameters as NIS+, but they clearly cannot accomplish the task of identifying causal emergence. (c) A comparison of the errors in multi-step predictions for different models trained on either partial (with 42,000 missing data points) or complete datasets. The test involves selecting 20 starting points within an area where the training samples are missing, evolving them for 10 steps using the learned macro-dynamics, and then decoding the results back into micro-states. The mean of the multi-step prediction errors for these 20 starting points is displayed. (d) A comparison is made between the two normalized vector fields of the SIR dynamics and the learned macro-dynamics. Each arrow represents a normalized direction and the magnitude of the dynamics' derivative at that coordinate point. In this experiment, to increase the accuracy of vector field prediction, we sample the raw trajectories every 20 time steps to form a new training set. The original vector fields without normalization can be referred to support information Figure 11.

generalization to unseen data. More details about experimental settings are shown in Support Information 7.3.

### 3.2. Boids

The second experiment is on Boids model which is a famous multi-agent model to simulate the collective behaviors of birds [39, 40]. In this experiment, we test the ability of NIS+ on capturing emergent collective behaviors and causal emergence quantification on different environments with intrinsic and extrinsic noises. To increase the explainability of the trained coarse-graining strategy, we also try to give an explicit correspondence between the learned macro-states and the micro-states.

In Boids model, the micro-state of each individual boid  $i$  is a four dimensional vector  $(x_i, y_i, v_{x,i}, v_{y,i})$ , where  $\mathbf{x}_i = (x_i, y_i)$  is the positional vector, and  $\mathbf{v}_i = (v_{x,i}, v_{y,i})$  is the velocity vector. Thus, the complete micro-state for all  $N$  boids is a  $4N$  dimensional vector. The micro-states follow the dynamical update equations:

$$\begin{cases} \mathbf{x}_i^{t+1} = \mathbf{x}_i^t + \mathbf{v}_i^t, \\ \mathbf{v}_i^{t+1} = \frac{\mathbf{v}_i^t + \Delta\mathbf{v}_i^t + \varepsilon_i^t}{\|\mathbf{v}_i^t + \Delta\mathbf{v}_i^t + \varepsilon_i^t\|} \|\mathbf{v}_i^t\|. \end{cases} \quad (7)$$

Where,  $\Delta\mathbf{v}_i^t$  is the external force exerted on  $i$  by its neighbors, and it is composed with three components which called cohesion, alignment, and separation, respectively, according to the dynamical rules of Boids model(see details in Support Information 7.4).  $\varepsilon_i^t = (\cos\Delta\alpha_i^t, \sin\Delta\alpha_i^t)^T$  is a force on turning direction exerted on each boid at each time step, where  $\Delta\alpha \in [-\pi, \pi]$  is a fixed value or random number.

We run the simulation with  $N = 16$  boids on a  $300 \times 300$  canvas, and all the boids are separated into two groups by forcing their  $\Delta\alpha_i^t$  as two distinct values  $\Delta\alpha_i^t \sim U(0.0058\pi, 0.0098\pi)$  for boids with  $i \leq 8$ , and  $\Delta\alpha_i^t \sim U(-0.0124\pi, -0.0084\pi)$  for boids  $i > 8$ . Therefore, the two groups will have separating trajectories with different turning angles as shown in Figure 4a. Causal emergence occurs for all tested dimensions( $q$ ) (see Figure 4e). With up to  $q = 8$  dimensional macro-state vectors, NIS+ can best capture the emergent collective flying behaviors of the two groups by tracing their centers of the trajectories. This can be visualized by decoding the predicted macro-states into the predicted micro-states as shown in Figure 4a by the two solid lines.

To enhance the interpretability of the learned coarse-graining function in NIS+, we utilize the Integrated Gradient (IG) method[41](see method section 5.5) to identify the most significant micro-states for each learned emergent macro-state dimension. We normalized the calculated IG and enhanced the maximum gradient of the micro-state in each macro-state and disregard the velocity dimensions of each boid due to their lower correlations with macro-states. The normalized IG is drawn into a matrix diagram(Figure 4d). As depicted by Figure 4d, the 1st, 2nd, 5th, and 6th dimensions in macro-states correspond to the boids in the first group (with  $ID < 8$ ), while the 3rd, 4th, 7th, and 8th dimensions correspond to the second group (with  $ID \geq 8$ ). Thus, the learned coarse-graining strategy uses two positional coordinates to represent all other information to form one dimension of macro-state.

To further validate that sparse micro-state dimensions can encode crucial information in dynamics, we intervene in the third dimension of the macroscopic state at the beginning, which corresponds to the x-axis coordinates of the second group of boids. This intervention allows us to observe the impact on the predicted behaviors by macro-dynamics, as shown in Figure 4c. Notably, we observe a horizontal shift in the predicted trajectories of the second group in Figure 4c. This also implies the dynamics-learner has learned a causal mechanism on the latent space of macro-states.

Furthermore, we conduct another set of experiments to see how the intrinsic and extrinsic noises can affect causal emergence. First, we suppose we cannot observe the micro-states  $(\mathbf{x}_i^t, \mathbf{v}_i^t)$ , but can read a noisy data  $(\mathbf{x}_i^{t'}, \mathbf{v}_i^{t'})$ , where  $\mathbf{x}_i^{t'} = \mathbf{x}_i^t + \delta \cdot \mathbf{x}_i^t$  and  $\mathbf{v}_i^{t'} = \mathbf{v}_i^t + \delta \cdot \mathbf{v}_i^t$ , in which  $\delta \sim \mathcal{N}(0, \delta_{max})$  is the extrinsic(observational) noise, and  $\delta_{max}$  is the parameter to control the level of this noise. Second, if we set  $\Delta\alpha \sim U(-\alpha \cdot \pi, \alpha \cdot \pi)$  as a random number evenly distributed in the interval of all possible angles, then  $\alpha \in [0, 1]$  controls the magnitude of the intrinsic noise because it affects the randomness of the dynamics.

As shown in Figure 4f and 4g, the mean absolute errors (MAEs) increase in both cases, indicating that the prediction tasks become more challenging as both intrinsic and extrinsic noises increase. However, the differences between the two types of noises can be observed by



examining the degrees of causal emergence ( $\Delta\mathcal{J}$ ). Figure 4f demonstrates that  $\Delta\mathcal{J}$  increases with the level of extrinsic noise ( $\delta_{max}$ ), suggesting that coarse-graining can mitigate the impact of noise within a certain range and enhance the causal effects. We have not included cases where  $\alpha > 0.6$  because the prediction errors (MAE) exceed the threshold  $\epsilon = 1$ . On the other hand, Figure 4g shows that  $\Delta\mathcal{J}$  decreases as the level of intrinsic noise ( $\alpha$ ) increases. This can be explained as the dynamics learner on the macro-level tries to capture the flocking behaviors of each group in this stage, but the flocking behaviors disappear gradually as the increase of intrinsic noise, thus the causal emergence decreases. Figure 4b shows real trajectories and the predictions for random deflection angle noise  $\alpha = 0.4$ . It can be seen that in the early stage, the straight-line trend can be predicted, but in the later stage, the deviation caused by noise gradually increases the error, which is the intuitive manifestation of the reduction in causal emergence. Therefore, we conclude that the coarse-graining operation can only eliminate the extrinsic(observational) noise but not the intrinsic(dynamical) noise. More details about the experiments of Boids can be referred to Support Information 7.4.

### 3.3. Game of Life

Conway’s Game of Life is a famous two dimensional cellular automata model on which various interesting dynamical patterns like glider, square, flower, signal light, honeycomb, traffic light emerge. Different from SIR model and Boids model, the micro-states of Game of Life at each time step are discrete(0 or 1) on a large regular grid as shown in Figure 5. Further, the micro-dynamics can not be represented by differential or difference equations but by rule tables (details can be referred to Support Information 7.5).

We show the power of NIS+ on capturing dynamical patterns. To finish this, we have to coarse-grain the micro-states of the cellular automata on both spatial and temporal dimensions because all the emergent patterns in Game of Life are dynamical. Therefore, to conduct this, we also demonstrate the flexibility of NIS+ by combining with other well-known neural computations like spatiotemporal convolution.

We extend the encoder( $\phi$ ) in NIS+ to realize a spatiotemporal coarse-graining strategy as shown in Figure 5(a). The entire coarse-graining process can be separated into two steps: the first step is to aggregate the information within a window with fixed size(3\*3 window in this paper) by simulating a convolutional neural network to get a spatial coarse-grained results; the second step then aggregates these results on multiple successive time steps to form a spatiotemporal coarse macro-state. All the information aggregation processes are implemented by parallel encoders of NIS+. After that forward and inverse dynamics learning on macro-states can be done. The decoding process can be finished by reversing the entire process of Figure 5(a).

Figures 5(c),(d) and (e) show the dynamical patterns that are generated by the ground truth simulations(the first row) and the predictions by NIS+(the third row), as well as the emergent macro-states that can make those predictions(the second row). We input two images with successive time steps into NIS+, and obtain another image pair with next two successive time steps. Compare the upper picture and lower ones, the patterns are very similar. That means, NIS+ can capture the patterns including moving, static, and oscillating structures.

We further test the degrees of causal emergence ( $\Delta\mathcal{J}$ ) on the trained models by different datasets with various pattern combinations as initial conditions. The results are shown in Figure 5(b), where, each bar represents a result of  $\Delta\mathcal{J}$  for one combination. For instance, ‘glider\_pattern’ means that the initial configuration is composed by a glider and a specific pattern(flowers, squares, and so forth). All the cases show that causal emergence have occurred, however, the degrees are higher for the combinations with same type of patterns, e.g., ‘glider\_glider’ and ‘pattern\_pattern’ cases. If the types are not same, e.g., ‘glider\_random’ or ‘glider\_perturb’, the degrees of causal emergence decreases as the patterns become random. We utilize the measure of causal emergence to select the optimal coarse-graining scales, and the results are presented in Support Information 7.5.3. These experiments demonstrate the effectiveness of the causal emergence measure in identifying interesting patterns and determining suitable hyperparameters.

We also evaluate the ability to capture dynamical patterns in various test environments that differ from the training environments, including different space sizes and varying numbers of gliders in the initial conditions. Both NIS and NIS+ are tested, and the results demonstrate that NIS+ outperforms NIS in capturing these patterns (refer to Support Information 7.5.2).

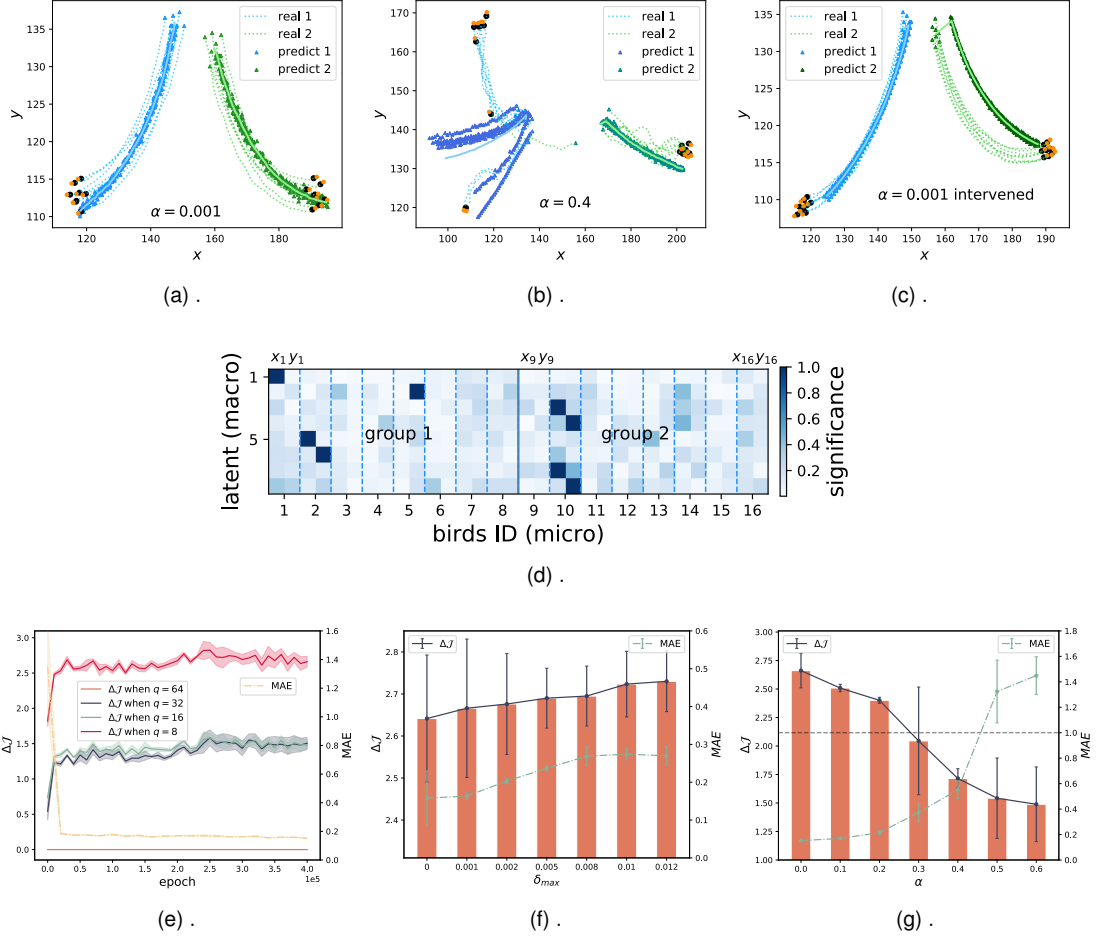


**Figure 4.** The experimental results of NIS+ on learning the collective flocking behaviors of the Boids model. (a) - (c) presents real and predicted data on boid trajectories under various conditions, (e) - (g) shows the changes in causal emergence ( $\Delta\mathcal{J}$ ) and loss (MAE) under different conditions. Concretely, (a) presents the comparison results between the real trajectories and the average results for multi-step (50 steps) predictions under the condition of two separating groups. (b) illustrates the real data and multi-step (50 steps) predictions for random deflection angles with a noise level of  $\alpha = 0.4$ . In (c), we demonstrate that after manually intervening in the third dimension of the learned macro-state, the predicted path of the right boid group shifted in the x-axis direction. (d) presents the saliency map, which visually depicts the association between each macroscopic dimension and the spatial coordinates of each boid. We highlight the most significant corresponding micro-states for each macro-state dimension with deep-blue dots, determined using the integrated gradients method applied to our model. The horizontal axis represents the  $x$  and  $y$  coordinates of 16 boids in the microscopic state, while the vertical axis represents the 8 macroscopic dimensions. The dodger-blue dashed line distinguishes the coordinates of different individual boids, while the steel-blue solid line separates the boid groups. (e) depicts the trend of dimension-averaged causal emergence changes with training epochs of NIS+ using different hyperparameters of  $q$ , which represents the scales of different macro-states. The optimized 8-dimensional macro-state exhibits a notable degree of causal emergence. In (f),  $\delta_{max}$  represents the standard deviation of the observational noise. The increase in observational noise within a certain range amplifies the degree of causal emergence, making it more pronounced. In (g), by adjusting the value of  $\alpha$ , we observe that as the random deflection angle increases, the degree of causal emergence gradually reduces. Simultaneously, the loss function for both the training and prediction data increases with  $\alpha$ . It is important to note that in these experiments, the threshold  $\epsilon$  is set to 1.0. Consequently, the results for  $\alpha > 0.4$  are not considered reliable due to the constraints defined in Equation 1 not being satisfied.

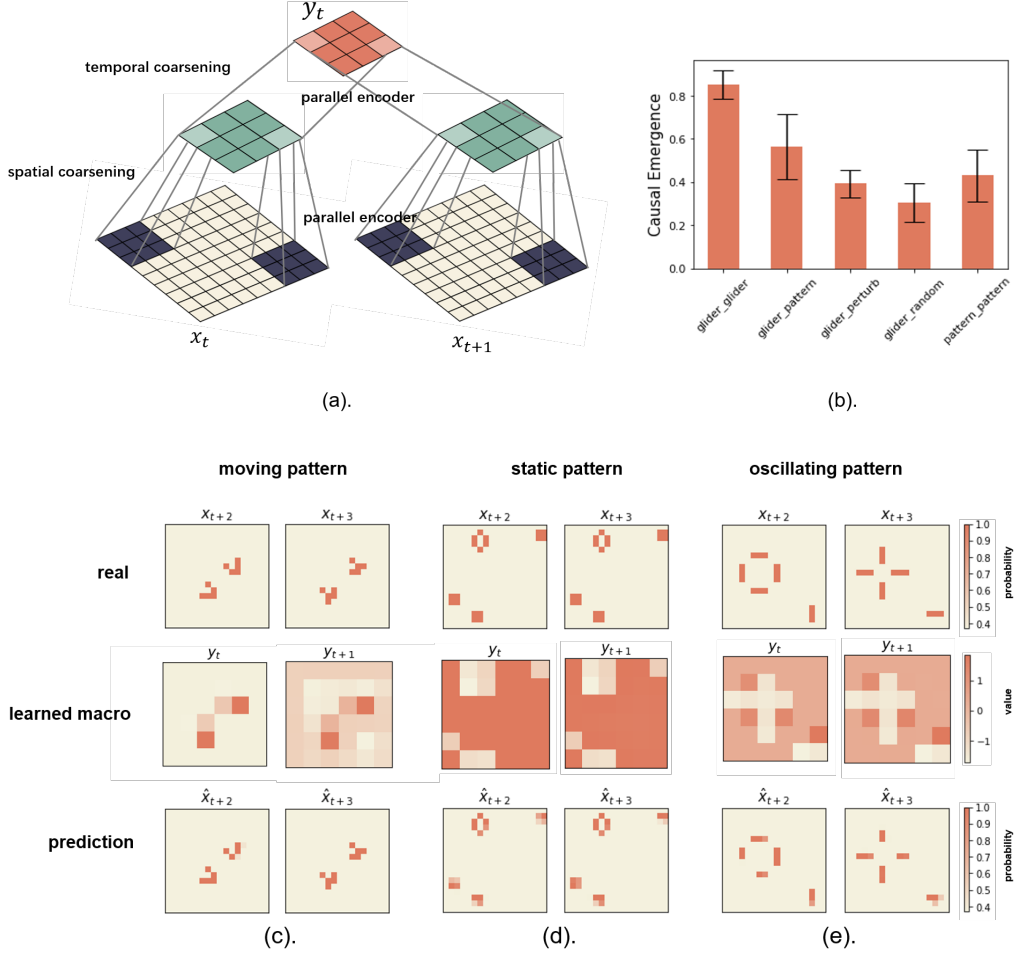


**Figure 5.** Experiments on the Game of Life. (a) The architecture of the encoder is illustrated, which can be divided into spatial encoding (mapping 3x3 grids to 1 grid) and temporal encoding (mapping 2 time steps to 1 step) stages. These processes are implemented using parallel encoders. (b) Comparisons of the degrees of causal emergence ( $\Delta\mathcal{J}$ , dimension averaged) are made among different models trained on datasets with various combinations of initial patterns. Each case represents a combination of two selected patterns as the initial image. For example, 'glider\_glider' indicates the combination of two gliders, 'glider\_pattern' represents a glider and another interesting pattern (such as static flowers, squares, or oscillating lights), 'glider\_perturb' represents a glider and a pattern with perturbations of the glider, 'glider\_random' represents a glider combined with a random pattern, and 'pattern\_pattern' indicates a model containing two interesting patterns. Each bar chart represents the average result of 3 experiments. (c), (d), and (e) depict the comparisons between the ground truth simulations, learned macro-states, and the predictions made by NIS+ for different patterns. In (c), the model is trained using images with gliders only. However, for (d) and (e), the training data is generated by simulating the Game of Life for 120 steps with random initial conditions, and only the images from steps 100-120 are selected to form the training set. The predicted images are the averaged results obtained by sampling from the predicted macro-states using the decoder 20 times. The colors in (d) and (e) represent the number of repetitions in the 20 samples.

### 3.4. Real fMRI time series data for brains

We also test NIS+ on real fMRI time series data of brains for 830 subjects. This experiment is different from other three cases because a set of real time series data with unknown dynamics for brains are fed into NIS+ to check whether causal emergence can be spotted and what emergent macro-level properties can be found to gain more understandings about the activities of brains for 830 subjects. Here, an open large fMRI dataset called AOMIC ID1000 is selected to serve as the real example[42]. This dataset collects subjects' fMRI scanning data while watching the same clip of movie. Thus, similar experiences of subjects under similar natural stimulus can be expected. Each time series of one individual subject emulates one sample of simulation for a dynamical system under a specific initial condition. This kind of setup is better than the time series data with long time steps but few samples(subjects) for NIS+ training. Further description about the dataset can be referred to method section.

After pre-processing of the raw time series through Schaefer atlas[43], we obtain a time series with 100 dimensions, of which each dimension corresponds to one functional brain area, as the observations of micro-states for each individual subject. All 830 time series for different subjects are divided into two groups, the first 800 time series are for training and the remaining 30 subjects' fMRI scan data for the test. The more details about setting and parameters of neural network in fMRI dataset can be seen in Table 7.7.

The results are shown in Figure 6(b). An evidently stronger causal emergence has been observed when  $q = 1$  which manifest we can represent the activities on different brain areas with one real number at each time step. This result can be confirmed by NIS framework for scale searching although the phenomenon that a stronger causal emergence when  $q = 1$  seems unstable. Also, we can see that  $q = 1$  also leads to comparatively better multi-step predictions(Figure 6e) while keeps a higher  $\Delta\mathcal{J}$ .

To examine how NIS+ coarse-grains the input data, we also employ the IG method to identify the most significant and least significant dimensions of the micro-state [41]. The partial results are presented in Figure 6d. We observe that the top 8 regions all belong to the visual (VIS) subnetworks (refer to Figure 6a and c). These visual subnetworks represent the functional system that the subjects utilized while watching movie clips.

While, we notice that the prediction results for these dimensions of micro-states within the VIS subnetwork and other associated regions are not necessarily better compared to the regions with lower averaged IG. The macro prediction from significant and insignificant regions exhibits distinct dynamic patterns (as shown in Figure 6d), which implies this is not a trivial solution.

Therefore, we can conclude that the complex dynamics of neural activities during movie watching can be encoded by a one-dimensional macro-state, primarily associated with the regions of the VIS subnetwork. This indicates that NIS+ is capable of learning to coarse-grain the complex fMRI signals from the brain and simulate the intricate dynamics using a single macro-state. Similar results can be obtained using alternative methods for data pre-processing, as demonstrated in the supporting information 7.6, suggesting the robustness of our findings.

## 4. Concluding Remarks

Inspired by the theory of causal emergence, this paper introduces a novel machine learning framework called Neural Information Squeezer Plus (NIS+) to discover interesting emergent patterns, macro-dynamics, and suitable coarse-graining methods directly from data. Additionally, it aims to quantify the degree of causal emergence under various conditions.

The distinguishing feature of our framework, compared to other machine learning frameworks, is its focus on maximizing the effective information (EI) of the learned macro-dynamics while maintaining effectiveness constraints. This allows the framework to learn a causal mechanism that is as independent as possible from the distribution of input data. This feature not only enables NIS+ to identify causal emergence in data across different environments but also enhances its ability for out-of-distribution generalization.

Four experiments were conducted to evaluate the capabilities of NIS+ in learning macro-dynamics, coarse-graining strategies, capturing emergent patterns, and quantifying causal emergence directly from data. These experiments encompassed three simulation scenarios: a simple dynamical system (SIR), a multi-agent system (Boid model), and a two-dimensional cellular automaton (Game of Life). Additionally, a real fMRI dataset generated from the brains of 830 human subjects while watching same movie clips was included as a fourth experiment.

The experiments demonstrate the ability of NIS+ to learn macro-dynamics effectively. The learned macro-dynamics not only accurately simulate the micro-dynamics observed in the data but also exhibit superior generalization capabilities when applied to out-of-training

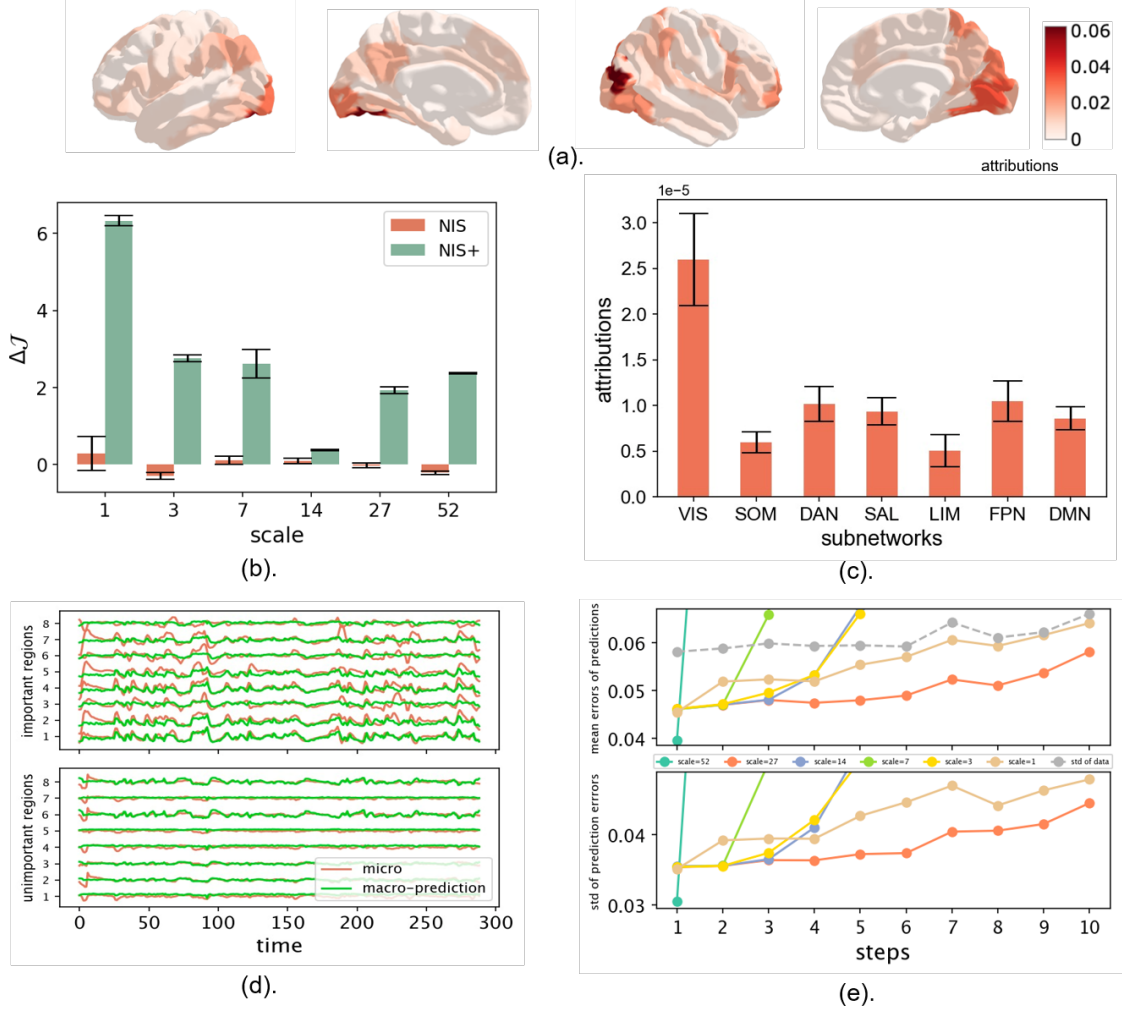


**Figure 6.** The learning results of fMRI data for the brains and the attribution analysis for the learned macro-state are presented. (a) Attribution maps, calculated using integrated gradient analysis of the encoder from the micro- to macro-scale with a scale of  $q = 1$ , are displayed. The maps show the left hemisphere from the view of the left, left hemisphere from the view of the right, right hemisphere from the view of the right, and right hemisphere from the view of the left. The colors represent the normalized absolute values of the integrated gradient. (b) Measures of causal emergence (dimension averaged) are compared among different models. It is evident that the NIS+ framework exhibits a substantial improvement in  $\Delta\mathcal{J}$ . The error bar represents the standard deviation. (c) The average attributions of subnetworks under the Schaefer Atlas are presented. The error bar represents the standard errors. (d) The time series visualization of the top and lowest 8 regions based on the attribution values (integrated gradient) is shown. (e) The mean errors of the multi-step predictions increase with the prediction steps under different scales ( $q$ ) on the test dataset. The grey dotted line represents the standard deviation of the data for comparison. The standard deviation of the prediction errors is also displayed below.

data. This out-of-distribution generalization ability is validated in the experiments involving the SIR model and the Game of Life model. The results indicate that by maximizing EI, NIS+ outperforms other machine learning models in tasks such as multi-step predictions and pattern capturing, even in environments that were not encountered during the training process. Consequently, NIS+ enables the acquisition of a more robust macro-dynamics in the latent space.

Furthermore, the experiment conducted on the Game of Life model demonstrates that NIS+ can effectively capture various emergent patterns, such as gliders and signal lights,

in different environments. Additionally, by measuring causal emergence, we can distinguish different scenarios in the data and identify which settings contain more regular patterns.

The process of coarse-graining a complex system can be effectively illustrated using the Integrated Gradients (IG) method, as demonstrated in the experiments involving the Boid model and the brain dataset. Through this method, the relationship between macro-states and micro-states can be visualized, allowing for the identification of the most significant variables within the micro-states. In the brain experiment, it was observed that the most crucial information stored in the unique macro-state exhibited a strong correlation with the micro-variables of the visual subnetwork. This finding highlights the ability of NIS+ to identify an appropriate coarse-graining strategy that aligns with meaningful biological interpretations.

The experiment conducted on the Boid model also sheds light on how two types of noise can impact the degrees of causal emergence. The results demonstrate that extrinsic noise, which arises from observational uncertainty, can be mitigated by the learned coarse-graining strategy. On the other hand, intrinsic noise, which stems from inherent uncertainty in the dynamical rules, cannot be eliminated. Furthermore, the degree of causal emergence increases with an increase in extrinsic noise, indicating that perturbing the observational data at the micro-level can lead to a better model with stronger causality at the macro-level. However, it is important to note that this may come at the cost of decreased prediction accuracy. Therefore, acquiring more data becomes crucial in order to strike a balance between capturing emergent patterns and maintaining prediction accuracy.

NIS+ holds potential for various applications in data-driven modeling of real complex systems, such as climate systems, collective behaviors, fluid dynamics, brain activities, and traffic flows. By learning more robust macro-dynamics, the predictive capabilities of these systems can be enhanced. For instance, El Niño, which arises from the intricate interplay of oceanic and atmospheric conditions, exemplifies the emergence of a major climatic pattern from underlying factors. Understanding these emergent macro-dynamics can be instrumental in modeling and predicting El Niño events. By leveraging NIS+ to capture and quantify the causal emergence in such complex systems, we can gain valuable insights and improve our ability to forecast their behavior.

Further extensions of the EI maximization method to other problem domains, such as image classification and natural language understanding, in addition to dynamics learning, warrant attention. Specifically, applying this principle to reinforcement learning agents equipped with world models has the potential to enhance performance across various environments. By incorporating the EI maximization approach into these domains, we can potentially improve the ability of models to understand and interpret complex visual and textual information. This can lead to advancements in tasks such as image recognition, object detection, language understanding, and machine translation.

The relationship between causal emergence and causal representation learning (CRL)[33] deserves further exploration. The NIS+ framework can be seen as a form of CRL, where the macro-dynamics serve as the causal mechanism and the coarse-graining strategy acts as the representation. As such, techniques employed in CRL can be applied to find causal emergence in data. Conversely, the concept of causal emergence and coarse-graining can be leveraged in CRL to enhance the interpretability of the model. By integrating the principles and methodologies from both causal emergence and CRL, we can potentially develop more powerful and interpretable models. This synergy can lead to a deeper understanding of the causal relationships within complex systems and enable the extraction of meaningful representations that capture the emergent patterns and causal mechanisms present in the data. Further research in this direction can contribute to advancements in both causal emergence and causal representation learning.

However, there are several limitations in this paper that should be addressed in future studies. Firstly, the requirement of a large amount of training data for NIS+ to learn the macro-dynamics and coarse-graining strategy may not be feasible in many real-world cases. Therefore, it is important to develop numerical methods that can estimate the degree of causal emergence directly from data without relying on extensive machine learning (ref [11] is a good example). Secondly, the interpretability of neural networks, particularly for the macro-dynamics learner, remains a challenge. Enhancing the interpretability of the learned models can provide valuable insights into the underlying mechanisms and improve the trustworthiness of the results. Additionally, the learned macro-dynamics in this work are homogeneous, resulting in the same EI value across different locations in the macro-state space. However, in real-world applications, this may not always hold true. Therefore, it is necessary to develop local measures for causal emergence, especially for systems with heterogeneous dynamics.



This would facilitate the identification of local emergent patterns, making the analysis more nuanced and insightful. Lastly, the current framework is primarily designed for Markov dynamics, while many real complex systems exhibit long-term memory or involve unobservable variables. Extending the framework to accommodate non-Markov dynamics is an important area for future research. Addressing these limitations and exploring these avenues for improvement will contribute to the advancement of the field and enable the application of NIS+ to a wider range of complex systems.

## 5. Methods and Data

In order to provide a comprehensive understanding of the article, we will first dedicate a certain amount of space to introduce Erik Hoel’s theory of causal emergence, and we introduce the details of the NIS and NIS+ frameworks and other used techniques. After that, the details of the fMRI time series data is introduced.

### 5.1. A Brief Introduction of Causal Emergence Theory

The basic idea of Hoel’s theory is that we have two different views (micro- and macro-) of a same Markov dynamical system, and causal emergence occurs if the macro-dynamics has stronger causal effect than the micro-dynamics. As shown in Figure 1, for example, the micro-scale system is composed by many colliding balls. The macro-scale system is a coarse-grained description of the colliding balls with colorful boxes where each box represents the number of balls within the box. In Figure 1, the vertical axis represents the scale(micro- and macro-), and the horizontal axis represents time, which depicts the evolution of the system’s dynamics in both scales. All the dynamical systems considered are Markovian, therefore two temporal successive snapshots are necessary. The dynamics in both micro- and macro-scales are represented by transitional probability matrix(TPM):  $f_m$  for micro-dynamics and  $f_M$  for macro-dynamics.

We can measure the strength of its causal effects for each dynamics(TPM) by effective information (EI). EI can be understood as an intervention-based version of mutual information between two successive states in a dynamical system over time. For any TPM  $f$ , EI can be calculated by:

$$\mathcal{J} = I(S_t; S_{t-1} | do(S_{t-1} \sim U(S))) = \frac{1}{N} \sum_{i,j=1}^N \left( f_{ij} \log f_{ij} - f_{ij} \log \left( \frac{\sum_{k=1}^N f_{kj}}{N} \right) \right), \quad (8)$$

where,  $S_t$  is the random variable to represent the state of the system at time  $t$ ,  $do(S_{t-1} \sim U(S))$  represents the do-operator [31] that intervene the state of the system at time  $t-1$  to force that  $S_{t-1}$  follows a uniform distribution on the value space  $S$  of  $S_t$ .  $f_{ij}$  is the probability at the  $i$ th row and the  $j$ th column.  $N = |S|$  is the total number of states and is also the number of rows or columns.  $\log$  represents the logarithmic operation with a base of 2. Equation 8 can be further decomposed into two terms: determinism and non-degeneracy which characterize that how the future state can be determined by the past state and vice versa, respectively[17].

With EI, we can compare two TPMs. If  $\mathcal{J}(f_M)$  is larger than  $\mathcal{J}(f_m)$ , we say causal emergence occurs in this dynamical system. In practice, we calculate another value called causal emergence (CE) to judge if causal emergence takes place, that is:

$$\Delta\mathcal{J} = \mathcal{J}(f_M) - \mathcal{J}(f_m). \quad (9)$$

Therefore, if  $\Delta\mathcal{J} > 0$ , then causal emergence occurs.  $\Delta\mathcal{J}$  can be treated as the quantitative measure of emergence for Markov dynamics. An example of causal emergence on Markov chain is shown in Figure 1(b).

### 5.2. Machine Learning Frameworks

We will introduce the details of the two frameworks NIS and NIS+ in this section.

#### 5.2.1. Neural Information Squeezer (NIS)

NIS use neural networks to parameterize all the functions to be optimized in Equation 1, in which the coarse-graining and anti-coarsening function  $\phi$  and  $\phi^\dagger$  are called encoder and decoder, respectively, and the macro-dynamics  $f_q$  is called dynamics-learner. Second, considering the symmetric position between  $\phi$  and  $\phi^\dagger$ , invertible neural network(with RealNVP

framework[44], details can be referred to the following sub-section) is used to reduce the model complexity and to make mathematical analysis being possible[12].

Concretely,

$$\phi \equiv Proj_q(\psi_\omega), \quad (10)$$

where  $\psi_\omega : \mathcal{R}^p \rightarrow \mathcal{R}^p$  is an invertible neural network with parameters  $\omega$ , and  $Proj_q$  represents the projection operation with the first  $q$  dimensions reserved to form the macro-state  $\mathbf{y}$ , and the last  $p - q$  dimensional variable  $\mathbf{y}'$  are dropped. Empirically,  $\mathbf{y}'$  can be approximately treated as a Gaussian noise and independent with  $\mathbf{y}$  or we can force  $\mathbf{y}'$  to be independent Gaussian by training the neural network. Similarly, in a symmetric way,  $\phi^\dagger$  can be approximated in the following way: for any input  $\mathbf{y} \in \mathcal{R}^q$ ,

$$\phi^\dagger(\mathbf{y}) = \psi_\omega^{-1}(\mathbf{y} \oplus \xi), \quad (11)$$

where  $\xi$  is a standard Gaussian random vector with  $p - q$  dimensions, and  $\oplus$  represents the vector concatenation operation.

Last, the macro-dynamics  $f_q$  can be parameterized by a common feed-forward neural network  $f_\theta$  with weight parameters  $\theta$ . Its number of input and output layer neurons equal to the dimensionality of the macro state  $q$ . It has two hidden layers, each with 64 neurons, and the output is transformed using LeakyReLU. Depending on the specific task, dynamics learner can be constructed using other types of neural networks. The detailed architectures and parameter settings of  $\psi_\omega$  and  $f_\theta$  can be referred to the supporting information (Support Information 7.7).

Previous work[12] has been proved that this framework merits many mathematical properties such as the macro-dynamics  $f_\theta$  forms an information bottleneck, and the mutual information between  $\mathbf{y}_t$  and  $\hat{\mathbf{y}}_{t+1}$  approximates the mutual information between  $\mathbf{x}_t$  and  $\mathbf{x}_{t+1}$  when the neural networks are convergent such that the constraint in Equation 1 is required.

### 5.2.2. Neural Information Squeezer Plus (NIS+)

To maximize EI defined in Equation 1, we extend the framework of NIS to form NIS+. In NIS+, we first use the formula of mutual information and variational inequality to convert the maximization problem of mutual information into a machine learning problem, and secondly, we introduce a neural network  $g_{\theta'}$  to learn the inverse macro-dynamics that is to use  $\mathbf{y}_{t+1} = \phi(\mathbf{x}_{t+1})$  to predict  $\mathbf{y}_t$  such that mutual information maximization can be guaranteed. Third, the probability re-weighting technique is employed to address the challenge of computing intervention for a uniform distribution, thereby optimizing the EI. All of these techniques compose neural information squeezer plus (NIS+).

Formally, the maximization problem under the constraint of inequality defined by Equation 1 can be converted as a minimization of loss function problem without constraints, that is:

$$\min_{\omega, \theta, \theta'} \sum_{t=1}^{T-1} w(\mathbf{x}_t) \|\mathbf{y}_t - g_{\theta'}(\mathbf{y}_{t+1})\| + \lambda \|\hat{\mathbf{x}}_{t+1} - \mathbf{x}_{t+1}\|, \quad (12)$$

where  $\omega, \theta, \theta'$  are the parameters of neural networks of  $\psi_\omega$ ,  $f_\theta$ , and  $g_{\theta'}$ , respectively.  $\mathbf{y}_t = \phi(\mathbf{x}_t) = Proj_q(\psi_\omega(\mathbf{x}_t))$  and  $\mathbf{y}_{t+1} = \phi(\mathbf{x}_{t+1}) = Proj_q(\psi_\omega(\mathbf{x}_{t+1}))$  are the macro-states.  $\lambda$  is a Lagrangian multiplier which will be taken as a hyper-parameter in experiments.  $w(\mathbf{x}_t)$  is the inverse probability weights which is defined as:

$$w(\mathbf{x}_t) = \frac{\tilde{p}(\mathbf{y}_t)}{p(\mathbf{y}_t)} = \frac{\tilde{p}(\phi(\mathbf{x}_t))}{p(\phi(\mathbf{x}_t))}, \quad (13)$$

where  $\tilde{p}$  is the new distribution of macro-states  $\mathbf{y}_t$  after intervention for  $do(\mathbf{y}_t \sim U_q)$ , and  $p$  is the natural distribution of the data. In practice,  $p(\mathbf{y}_t)$  is estimated through kernel density estimation (KDE)[38](Please refer section 5.4). The approximated distribution,  $\tilde{p}(\mathbf{y}_t)$ , is assumed to be a uniform distribution, which is characterized by a constant value. Consequently, the weight  $w$  is computed as the ratio of these two distributions.

We can prove a mathematical theorem to guarantee such problem transformation as mentioned below:

**Theorem 5.1** (Problem Transformation Theorem). *For a given value of  $q$ , assuming that  $\omega^*, \theta^*$ , and  $\theta'^*$  are the optimal solutions to the unconstrained objective optimization problem defined by equation (12). Then  $\phi^* \equiv Proj_q(\psi_{\omega^*})$ ,  $f_q^* \equiv f_{\theta^*}$ , and  $\phi^{\dagger,*}(\cdot) \equiv \psi_{\omega^*}^{-1}(\cdot \oplus \xi)$ , where  $\xi \sim \mathcal{N}(0, I_{p-q})$  are the optimal solution to the constrained objective optimization problem Eq.(1).*

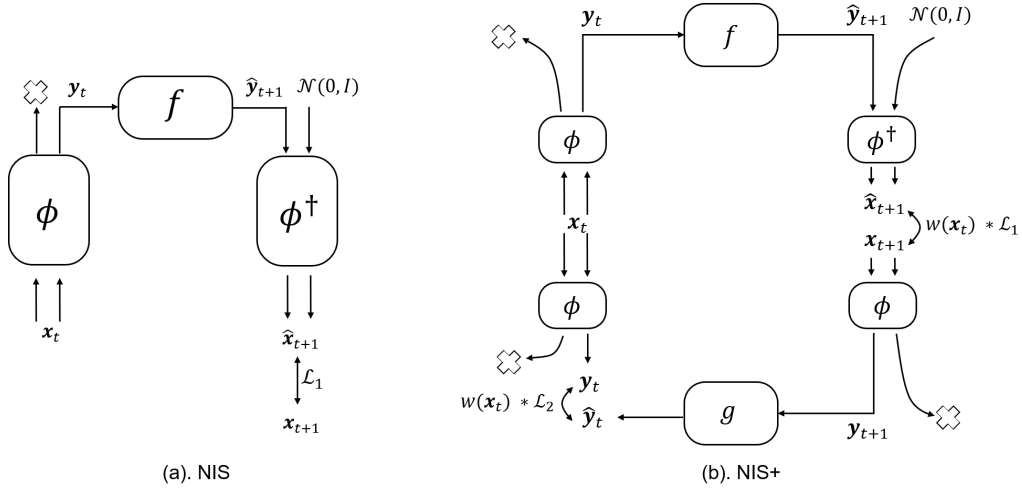


**Figure 7.** The frameworks of NIS (a) and NIS+ (b). The boxes in the diagram represent functions or neural networks, while the arrow pointing to a cross signifies the operation of information dropping.  $x_t$  and  $x_{t+1}$  represent the observational data of micro-states, and  $\hat{x}_{t+1}$  represents the predicted micro-state. The macro-states, denoted as  $y_t = \phi(x_t)$  and  $y_{t+1} = \phi(x_{t+1})$ , are obtained by encoding the micro-states using the encoder. Similarly, the predicted macro-states,  $\hat{y}_t = \phi(\hat{x}_t)$  and  $\hat{y}_{t+1} = \phi(\hat{x}_{t+1})$ , are obtained by encoding the predictions of micro-states.

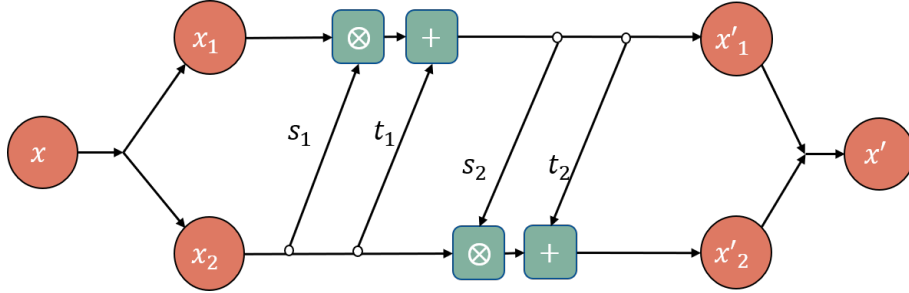


**Figure 8.** Structure diagram of RealNVP.

The details of proof can be seen in Support Information 7.2.1.

Discriminate from Figure 7(a), a new computational graph for NIS+ which is depicted in Figure 7(b) is implied by the optimization problem defined in Equation 12. For given pair of data:  $x_t, x_{t+1}$ , two dynamics, namely the forward dynamics  $f_\theta$  and the reverse dynamics  $g_{\theta'}$  are trained by optimizing two objective functions  $\mathcal{L}_1 = \sum_{t=1}^{T-1} w(x_t) \|y_t - g_{\theta'}(y_{t+1})\|$  and  $\mathcal{L}_2 = \sum_{t=1}^{T-1} \lambda \|\hat{x}_{t+1} - x_{t+1}\|$ , simultaneously. In the training process, the encoder,  $\phi$  and the decoder,  $\phi^\dagger$  are shared.

This novel computational framework of NIS+ can realize the maximization of EI under the coarse-grained emergent space. Therefore, it can optimize an independent causal mechanism( $f$ ) represented by  $f_\theta$  on the emergent space. It can also be used to quantify causal emergence in raw data once the macro-dynamics  $f_\theta$  is obtained for different  $q$ .

### 5.2.3. Invertible neural network in encoder(decoder)

In NIS, both the encoder( $\phi$ ) and the decoder( $\phi^{dag}$ ) use the invertible neural network module RealNVP[44].

Concretely, if the input of the module is  $\mathbf{x}$  with dimension  $p$  and the output is  $\mathbf{x}'$  with the same dimension, then the RealNVP module can perform the following computation steps:

$$\begin{cases} \mathbf{x}_1 = \mathbf{x}_{1:m} \\ \mathbf{x}_2 = \mathbf{x}_{m:p} \end{cases} \quad (14)$$

where,  $m$  is an integer in between 1 and  $p$ .

$$\begin{cases} \mathbf{x}'_1 = \mathbf{x}_1 \otimes s_1(\mathbf{x}_2) + t_1(\mathbf{x}_2) \\ \mathbf{x}'_2 = \mathbf{x}_2 \otimes s_2(\mathbf{x}'_1) + t_2(\mathbf{x}'_1) \end{cases} \quad (15)$$

where,  $\otimes$  is element-wised time,  $s_1, s_2, t_1$  and  $t_2$  are feed-forward neural networks with arbitrary architectures, while their input-output dimensions must match with the data. For the experiments in this article, they each have two intermediate hidden layers. The input and output layers have the same number of neurons as the dimensions of the micro-state samples. Each hidden layer has 64 neurons, and the output of each hidden layer is transformed by the non-linear activation function LeakyReLU. In practice,  $s_1$  or  $s_2$  always do an exponential operation on the output of the feed-forward neural network to facilitate the inverse computation.

Finally,

$$\mathbf{x}' = \mathbf{x}'_1 \oplus \mathbf{x}'_2 \quad (16)$$

It is not difficult to verify that all three steps are invertible. Equation 15 is invertible because the same form but with negative signs can be obtained by solving the expressions of  $\mathbf{x}_1$  and  $\mathbf{x}_2$  with  $\mathbf{x}'_1$  and  $\mathbf{x}'_2$  from Equation 15.

To simulate more complex invertible functions, we always duplex the basic RealNVP modules by stacking them together. In the main text, we use duplex the basic RealNVP module by three times.

Due to the reversibility of RealNVP, if its output is used as input in a subsequent iteration, the new output will be the same as the original input. Therefore, the neural networks used in the encoder-decoder can share parameters. The process of encoding to obtain the macro-state involves projecting the forward output and retaining only the first few dimensions. On the other hand, the process of decoding to obtain the micro-state involves concatenating the macro-state with a normal distribution noise, expanding it to match the micro-state dimensions, and then feeding it back into the entire invertible neural network.

#### 5.2.4. Extensions for Practical Computations

When we apply NIS+ to the data generated by various complex systems such as cellular automata and multi-agent systems, the architecture of encoder(decoder) should be extended for stacked and parallel structures. Fortunately, NIS+ is very flexible to different real scenarios which means the important properties such as Theorem 5.1 can be retained.

Firstly, it is important to consider that when dealing with high-dimensional complex systems, discarding multiple dimensions at once can pose challenges for training neural networks. Therefore, we replace the encoder in NIS+ with a **Stacked Encoder**. As shown in Figure 9(a), this improvement involves stacking a series of basic encoders together and gradually discard dimensions, thereby reducing the training difficulty.

In addition, complex systems like cellular automata are always comprise with multiple components with similar dynamical rules. Therefore, we introduce the **Parallel Encoder** to represent each component or groups of these components and combine the results together. Concretely, as shown in Figure 9(b), inputs may be grouped based on their physical relationships(e.g. adjacent neighborhood), and each group is encoded using a basic encoder. By sharing parameters among the encoders, neural networks can capture homogeneous coarse-graining rules efficiently and accurately. Finally, the macro variables obtained from all the encoders are concatenated into a vector to derive the overall macro variables. Furthermore, we can combine this parallel structures with other well-known architectures like convolutional neural networks.

To enhance the efficiency of searching for the optimal scale, we leverage the multiple scales of hidden space obtained through the stacked encoder by training multiple dynamics learners in different scales simultaneously. This forms the framework of **Multistory NIS+** as shown in Figure 9(c). This approach is equivalent to searching macro-dynamics for different  $q$  and thereby avoiding to retrain the encoders.

Theorem 5.2 guarantee that the important properties such as Theorem 5.1 can be retained for the extensions of stacked and parallel encoders. And a new universal approximation theorem (Theorem 5.3) can be proved such that multiple stacked encoders can approximate any coarse-graining function (any map defined on  $\mathcal{R}^p \times \mathcal{R}^q$ ).

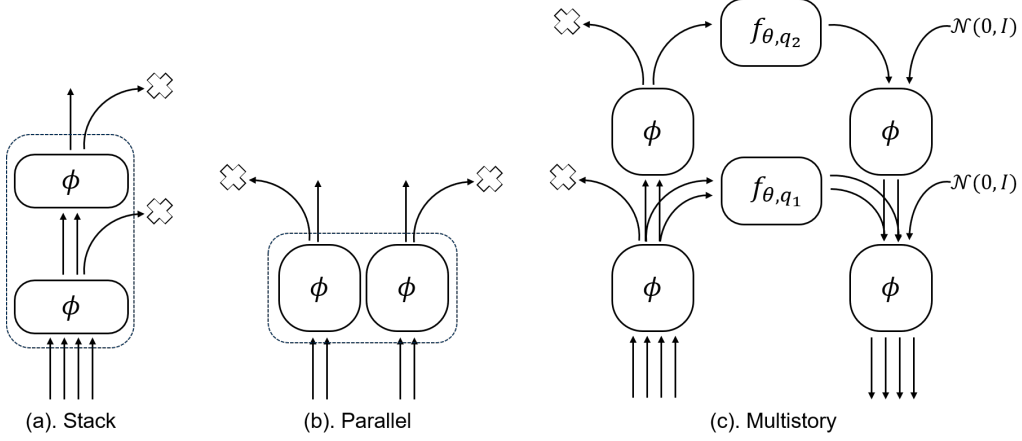


**Figure 9.** Three extended structures of the NIS+ encoder, denoted as (a) and (b), as well as the complete structure (c), are designed to facilitate the implementation of complex tasks. (a) represents a stacked encoder, where basic encoders are layered one on top of another. This arrangement allows for the filtering of input information in a hierarchical manner. (b) showcases a parallel encoder, where multiple basic encoders with shared parameters are combined to form a larger encoder. This parallel configuration enables the processing of input information in parallel, enhancing efficiency. (c) illustrates a multistory structure of the complete NIS+ framework. In this structure, the encoders and decoders are stacked, and the dynamics learners in different layers operate in parallel. This design facilitates simultaneous training for different dynamics learners with distinct dimensions and enables parallel searching for the optimal dimension  $q$ .

**Theorem 5.2** (Problem Transformation in Extensions of NIS+ Theorem). *When the encoder of NIS+ is replaced with an arbitrary combination of stacked encoders and parallel encoders, the conclusion of Theorem 2.1 still holds true.*

**Theorem 5.3** (Universal Approximating Theorem of Stacked Encoder). *For any continuous function  $f$  which is defined on  $K \times \mathcal{R}^p$ , where  $K \in \mathcal{R}^p$  is a compact set, and  $p > q \in \mathbb{Z}^+$ , there exists an integer  $s$  and an extended stacked encoder  $\phi_{p,s,q} : \mathcal{R}^p \rightarrow \mathcal{R}^q$  with  $s$  hidden size and an expansion operator  $\eta_{p,s}$  such that:*

$$\phi_{p,s,q} \simeq f, \quad (17)$$

Thereafter, an extended stacked encoder with expansion operators is of universal approximation property which means that it can approximate and simulate any coarse-graining function defined on  $\mathcal{R}^p \times \mathcal{R}^q$ .

The extended stacked encoder  $\phi_{p,s,q}$  refers to stacking two basic encoders together and gradually reducing dimensions, encoding the input from  $p$  dimensions to  $q$  dimensions, with an intermediate dimension of  $s$ . Besides basic operations such as invertible mapping and projection, a new operation, vector expansion( $\eta_{p,s}$ , e.g.,  $\eta_{2,5}(1, 2, 3) = (1, 2, 3, 1, 2)$ ), should be introduced, and locate in between the two encoders. All the proves of these theorems are referred to Supporting Information 7.2.2 and 7.2.3.

### 5.2.5. Training NIS+

In practice, two stages are separated during training process for NIS+ and all extensions. The first stage only trains the forward neural networks (the upper information channel as shown in Figure 2) such that the loss  $\mathcal{L}_1$  is small enough. Then, the second stage which only trains the neural networks for the reverse dynamics (the lower information channel as shown in Figure 2) is conducted. Because the trained inverse dynamics  $g_{\theta'}$  is never used, the second stage is for training  $\phi_{\omega}$  in essence.

### 5.3. Measures and calculations of EI and causal emergence for neural networks

The measure of EI of discrete Markov chains can be calculated by Equation 8, however, it is not suitable for neural networks because a neural network is a deterministic function.

Therefore, we need to extend the definition of EI for general neural networks. We continue to use the method defined in [12]. The basic idea is to understand a neural network as a Gaussian distribution conditional on the input vector with the mean as the deterministic function of the input values, and the standard deviations as the mean square errors of this neural network on the training or test datasets.

In general, if the input of a neural network is  $X = (x_1, x_2, \dots, x_n) \in [-L, L]^n$ , which means  $X$  is defined on a hyper-cube with size  $L$ , where  $L$  is a very large integer. The output is  $Y = (y_1, y_2, \dots, y_m)$ , and  $Y = \mu(X)$ . Here  $\mu$  is the deterministic mapping implemented by the neural network:  $\mu : \mathcal{R}^n \rightarrow \mathcal{R}^m$ , and its Jacobian matrix at  $X$  is  $\partial_{X'} \mu(X) \equiv \left\{ \frac{\partial \mu_i(X')}{\partial X'_j} \Big|_{X'=X} \right\}_{nm}$ . If the neural network can be regarded as a Gaussian distribution conditional on given  $X$ , then the effective information (EI) of the neural network can be calculated in the following way:

$$EI_L(\mu) = I(\text{do}(X \sim U([-L, L]^n); Y)) \approx -\frac{m + m \ln(2\pi) + \sum_{i=1}^m \sigma_i^2}{2} + n \ln(2L) + \mathbf{E}_{X \sim U([-L, L]^n)} (\ln |\det(\partial_{X'} \mu(X))|). \quad (18)$$

where,  $\Sigma = \text{diag}(\sigma_1^2, \sigma_2^2, \dots, \sigma_m^2)$  is the co-variance matrix, and  $\sigma_i$  is the standard deviation of the output  $y_i$  which can be estimated by the mean square error of  $y_i$  under given  $x_i$ .  $U([-L, L]^n)$  is the uniform distribution on  $[-L, L]^n$ , and  $|\cdot|$  is absolute value, and  $\det$  is determinant. If  $\det(\partial_{X'} \mu(X)) \equiv 0$  for all  $X$ , then we set  $EI \approx 0$ .

However, Equation 18 can not be applied in real cases directly because it will increase as the dimension of input  $n$  or output  $m$  increases[12]. Therefore, larger EI is always expected for the models with higher dimension. The way to solve this problem is by dividing the input dimension to define dimension averaged effective information(dEI) and is denoted as  $\mathcal{J}$ :

$$\mathcal{J}_L = \frac{EI_L(\mu)}{n} \quad (19)$$

When the numbers of input and output are identical ( $m = n$ , this condition is always hold for all the results reported in the main text), Equation 18 becomes:

$$\mathcal{J}_L(\mu) = -\frac{1 + \ln(2\pi) + \sum_{i=1}^n \sigma_i^2/n}{2} + \ln(2L) + \frac{1}{n} \mathbf{E}_{X \sim U([-L, L]^n)} (\ln |\det(\partial_{X'} f(X))|). \quad (20)$$

We always use this measure to quantify EI for neural networks in the main text. However, this measure is also not perfect because it is dependent on a free parameter  $L$ , the range of the domain for the input data. Our solution is to calculate the dimension averaged causal emergence to eliminate the influence of  $L$ . For macro-dynamics  $f_M$  with dimension  $q$  and micro-dynamics  $f_m$  with dimension  $p$ , we define dimension averaged causal emergence as:

$$\Delta \mathcal{J}_L(f_M, f_m) = \mathcal{J}_L(f_M) - \mathcal{J}_L(f_m) = \frac{EI_L(f_M)}{q} - \frac{EI_L(f_m)}{p}. \quad (21)$$

If  $f_M$  and  $f_m$  are parameterized by neural networks of  $\mu_M$  with dimension  $q$  and  $\mu_m$  with dimension  $p$ , then

$$\Delta \mathcal{J} = \left( \frac{1}{q} \mathbf{E}_{X_M} \ln |\det \partial_{X_M} \mu_M| - \frac{1}{p} \mathbf{E}_{X_m} \ln |\det \partial_{X_m} \mu_m| \right) - \left( \frac{1}{q} \sum_{i=1}^q \ln \sigma_{i,M}^2 - \frac{1}{p} \sum_{i=1}^p \ln \sigma_{i,m}^2 \right), \quad (22)$$

where  $\sigma_{i,M}$  and  $\sigma_{i,m}$  are the standard deviations for  $\mu_M$  and  $\mu_m$  on the  $i$ th dimension, respectively. At this point, the influences of the input or output dimensions and the parameter  $L$  has been completely eliminated, making it a more reliable indicator. Therefore, the comparisons between the learned macro-dynamics reported in the main text are reliable because the measure of dimension averaged causal emergence is used.

In practice, the first step is to select a sufficiently large value for  $L$  to ensure that all macro-states are encompassed within the region  $[-L, L]^q$ . Subsequently, the determinant of Jacobian matrices can be estimated using Monte Carlo integration, which involves sampling data points within this region. The standard deviations can be estimated using a test dataset, and the probability reweighting technique is employed to account for interventions and ensure a uniform distribution.



#### 5.4. KDE for probability reweighting

In order to use inverse probability weighting technique, we need to estimate the probability distribution of the samples. KDE(Kernel Density Estimation) is a commonly used estimation method that can effectively eliminate the influence of outliers on the overall probability distribution estimation. In this experiment, we estimate the probability distribution of macro-states  $\mathbf{y}_t$ . Below is an introduction to the operation details of KDE. For a sample  $(x_1, x_2, \dots, x_n)$ , we have the following kernel density estimation:

$$\hat{f}_h(x) = \frac{1}{nh} \sum_{i=1}^n K\left(\frac{x - x_i}{h}\right). \quad (23)$$

$n$  represents the number of samples, the hyperparameter  $h$  denotes the bandwidth, which is determined based on the rough range of the data and typically set to 0.05 in this article.  $K$  is the kernel, specifically the standard normal density function. After obtaining the estimation function, each sample point is evaluated individually, resulting in the corresponding probability value for each sample point. By dividing the probability of the target distribution (uniform distribution) by our estimated probability value, we obtained the inverse probability weights corresponding to each sample point. To cover all sample points, the range of the uniform distribution needs to be limited by a parameter  $L$ , which ensures that a square with side length  $2L$  can encompass all the sample points in all dimensions.

Another thing to note is that the weights obtained at this point are related to the sample size, so they need to be normalized. However, this will result in very small weight values corresponding to the samples. Therefore, it is necessary to multiply them by the sample quantity to amplify the weight values back to their normal scale. Then, multiply this weight value by the training loss of each sample to enhance the training of sparse regions, achieving the purpose of inverse probability weighting. Since the encoder parameters change with each iteration, causing the distribution of  $\mathbf{y}_t$  to change, we will re-estimate the probability distribution of the entire sample using KDE every 1000 epochs (a total of at least 30000 epochs of iteration, the number of iterations may vary in different experiments).

#### 5.5. Integrated Gradients for attribution

Here we introduce a method called Integrated Gradients[45] that is used to explain the connection between macro-states and micro-states. To formally describe this technique, let us consider a function  $F : \mathcal{R}^p \rightarrow [0, 1]$  that represents a deep network. Specifically, let  $x \in \mathcal{R}^p$  denote the input under consideration, and  $x' \in \mathcal{R}^p$  denote the baseline input. In both the fMRI and Boids experiments, the baseline is set to 0.

We compute the gradients at each point along a straight-line path (in  $\mathcal{R}^p$ ) from the baseline  $x'$  to the input  $x$ . By accumulating these gradients to obtain the final measure of integrated gradients(IG). More precisely, integrated gradients are defined as the path integral of the gradients along the straight-line path from the baseline  $x'$  to the input  $x$ .

The integrated gradient along the  $i$ -th dimension for an input  $x$  and baseline  $x'$  is defined as follows. Here,  $\partial F(x)/\partial x_i$  represents the gradient of  $F(x)$  along the  $i$ -th dimension. The Integrated Gradients(IG) that we have computed are shown in Equation 24.

$$IG_i(x) = (x_i - x'_i) \times \int_{\alpha=0}^1 \frac{\partial F(x' + \alpha \times (x - x'))}{\partial x_i} d\alpha. \quad (24)$$

#### 5.6. fMRI time series data description in detail

AOMIC ID1000 is an fMRI dataset collected when 881 subjects are watching movies. It contains both raw data and preprocessed data(See more experimental and preprocessing details in [42]). Here, we should notice that the movie is edited in a way for no clear semantic meanings but just some concatenated images from the movie. Therefore, it is expected that subjects' brain activation patterns shouldn't respond to some higher-order functions such as semantic understandings.

When working with fMRI data, the high dimensionality of the data (over 140,000 dimensions) poses computational challenges. To address this, dimension reduction techniques through brain atlas are employed to make the calculations feasible. We first preprocessed the data by removing the effects of artificial motion, global signal, and white matter signal and cerebrospinal fluid signal using fmriPrep results contained in AOMIC ID1000[46, 47]. Simultaneously, we detrend and normalize the data during this process. By doing the whole preprocessing process, we also throw out 51 subjects' data since some time steps of these

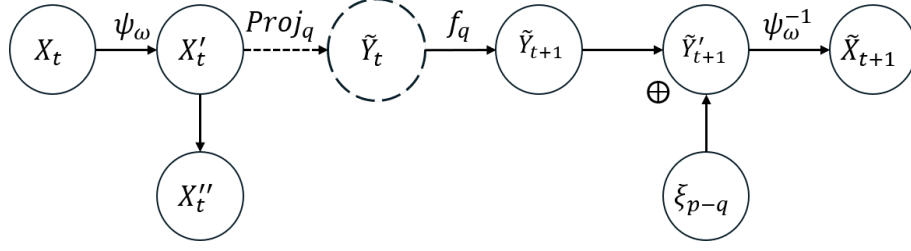


**Figure 10.** The causal graph among random variables after intervention on  $Y_t$  according to the framework of NIS or NIS+. Because the intervention on  $Y_t$  can only affect the variables in the upper part of NIS+ framework, we ignore the variables in the lower part. In the diagram,  $X'_t$  represents the random variable obtained after reversible transformation of  $X_t$ ,  $X''_t$  represents the variable directly discarded during the projection process,  $\tilde{Y}'_{t+1}$  represents a new variable composed of  $\tilde{Y}_{t+1}$  concatenated with a standard normal distribution, and  $\xi_{p-q}$  represents a  $p-q$  dimensional standard normal distribution. The dashed circular shape in the diagram represents the variable that is directly intervened to a uniform distribution, and the dashed arrow represents the causal relationship that is severed due to the intervention.

subject's have been removed. Furthermore, to facilitate the investigation of the correlation between the required brain function for watching movie clips and the emergent macro dynamics, we employed the Schaefer atlas to divide the brain into 100 functional areas. Also, we have committed the philosophy of anatomical Atlas, which seems to suggest the converging evidence(See 7.6). All of these preprocessing steps were performed using Nilearn[48, 49].

## 6. Acknowledgement

The authors would like to acknowledge all the members who participated in the "Causal Emergence Reading Group" organized by the Swarma Research and the "Swarma - Kaifeng" Workshop. We are especially grateful to Professors Yizhuang You, Peng Cui, Dr. Chaochao Lu, and Dr. Yanbo Zhang for their invaluable contributions and insightful discussions throughout the research process.

## 7. Support Information

### 7.1. Preceding instructions

Before we prove the theorem, let us first introduce the symbols that will be used in the following paragraphs. We will use capital letters to represent the corresponding random variables. For example,  $X_t$  represents the random variable of the micro-state  $\mathbf{x}_t$  at time  $t$ , and  $Y_{t+1}$  represents the random variable corresponding to the macro-state  $\mathbf{y}_{t+1}$ . For any random variable  $X$ ,  $\tilde{X}$  represents the same random variable  $X$  after intervention.  $\hat{X}$  means the prediction for  $X$  given by neural networks.

Second, to understand how the intervention on  $Y_t$  can affect other variables, a causal graph derived from the framework of NIS and NIS+ and depicts the causal relations among variables is very useful, this is shown in Figure 10. In which,  $X_t$  and  $\tilde{X}_{t+1}$  denote the input random variable and predicted output random variable of the NIS+ on a micro scale, while  $Y_t$  and  $\hat{Y}_{t+1}$  represent the input and output of  $f_q$  on a macro scale. After intervening on  $Y_t$ ,  $\tilde{X}_t$ ,  $\tilde{X}_{t+1}$ ,  $\tilde{Y}_t$ ,  $\tilde{Y}_{t+1}$  represent different micro or macro variables under the intervention  $do(Y_t \sim U(Y))$ , corresponding to  $X_t$ ,  $\tilde{X}_{t+1}$ ,  $Y_t$ , and  $\hat{Y}_{t+1}$ , respectively.

### 7.2. Mathematical Proves

In this sub-section, we will show the mathematical proves of the theorems mentioned in the main text.

#### 7.2.1. Proof of Theorem 5.1

To prove this theorem, we utilize a combination of the inverse macro-dynamic and probability re-weighting technique, along with information theory and properties of neural networks. In this proof, we need three lemmas, stated as follows:

**Lemma 7.1** (Bijection mapping does not affect mutual information). *For any given continuous random variables  $X$  and  $Z$ , if there is a bijection (one to one) mapping  $f$  and another random variable  $Y$  such that for any  $x \in \text{Dom}(X)$  there is a  $y = f(x) \in \text{Dom}(Y)$ , and vice versa, where  $\text{Dom}(X)$  denotes the domain of the variable  $X$ , then the mutual information between  $X$  and  $Z$  is equal to the information between  $Y$  and  $Z$ , that is:*

$$I(X; Z) = I(Y; Z), \quad (25)$$

**Lemma 7.2** (Mutual information will not be affected by concatenating independent variables). *If  $X \in \text{Dom}(X)$  and  $Y \in \text{Dom}(Y)$  form a Markov chain  $X \rightarrow Y$ , and  $Z \in \text{Dom}(Z)$  is a random variable which is independent on both  $X$  and  $Y$ , then:*

$$I(X; Y) = I(X; Y \oplus Z). \quad (26)$$

The proofs of Lemma 7.2 and Lemma 7.1 can be found in the reference [12].

**Lemma 7.3** (variational upper bound of a conditional entropy). *Given a conditional entropy  $H(\mathbf{y}|\mathbf{x})$ , where  $\mathbf{x} \in \mathcal{R}^s$ ,  $\mathbf{y} \in \mathcal{R}^q$ , there exists a variational upper bound on this conditional entropy:*

$$H(Y|X) \leq - \iint p(\mathbf{y}, \mathbf{x}) \ln g(\mathbf{y}|\mathbf{x}) d\mathbf{y} d\mathbf{x}, \quad (27)$$

where  $g(\mathbf{y}|\mathbf{x}) \in \mathcal{R}^q \times \mathcal{R}^s$  is any distribution.

*Proof.* First, we unfold the conditional entropy

$$H(Y|X) = - \iint p(\mathbf{x}) p(\mathbf{y}|\mathbf{x}) \ln p(\mathbf{y}|\mathbf{x}) d\mathbf{y} d\mathbf{x} \quad (28)$$

Due to the property of KL divergence[50], for any distribution  $g$ ,

$$D_{KL}(p||g) = \int p(\mathbf{x}) \ln \frac{p(\mathbf{x})}{g(\mathbf{x})} d\mathbf{x} \geq 0. \quad (29)$$

On the other words,

$$\int p(\mathbf{x}) \ln p(\mathbf{x}) d\mathbf{x} \geq \int p(\mathbf{x}) \ln g(\mathbf{x}) d\mathbf{x}. \quad (30)$$

So,

$$\begin{aligned} H(\mathbf{y}|\mathbf{x}) &= - \int p(\mathbf{x}) \int p(\mathbf{y}|\mathbf{x}) \ln p(\mathbf{y}|\mathbf{x}) d\mathbf{y} d\mathbf{x} \\ &\leq - \int p(\mathbf{x}) \int p(\mathbf{y}|\mathbf{x}) \ln g(\mathbf{y}|\mathbf{x}) d\mathbf{y} d\mathbf{x} \\ &= - \iint p(\mathbf{y}, \mathbf{x}) \ln g(\mathbf{y}|\mathbf{x}) d\mathbf{y} d\mathbf{x}. \end{aligned} \quad (31)$$

□

To prove the theorem, we also use an assumption:

**Assumption:** The composition of the inverse dynamics  $g_{\theta'}$  and the encoder  $\phi$  can be regarded as a conditional probability  $P(\hat{Y}_{t+1}|X_t)$ , and this probability can be approximated as a Gaussian distribution  $N(g_{\theta'}(\phi(\mathbf{x}_{t+1})), \Sigma)$ , where  $\Sigma = \text{diag}(\sigma_1, \sigma_2, \dots, \sigma_q)$ , and  $\sigma_i$  is the MSE loss of the  $i$ th dimension of output  $\hat{Y}_{t+1}$ . Further, suppose  $\sigma_i$  is bounded, thus  $\sigma_i \in [\sigma_m, \sigma_M]$  for any  $i$ , where  $\sigma_m$  and  $\sigma_M$  are the minimum and maximum values of MSEs.

This assumption is supported by the reference [51].

Next, we restate the theorem that needs to be proved:

**Theorem 5.1** (Problem Transformation Theorem): For a given value of  $q$ , assuming that  $\omega^*$ ,  $\theta^*$ , and  $\theta'^*$  are the optimal solutions to the unconstrained objective optimization problem defined by equation (12). Then  $\phi^* \equiv \text{Proj}_q(\psi_{\omega^*})$ ,  $f_q^* \equiv f_{\theta^*}$ , and  $\phi^{\dagger,*}(\cdot) \equiv \psi_{\omega^*}^{-1}(\cdot \oplus \xi)$ , where  $\xi \sim \mathcal{N}(0, I_{p-q})$  are the optimal solution to the constrained objective optimization problem Eq.(1).

*Proof.* The original constrained goal optimization framework is as follows:

$$\begin{aligned} & \max_{\phi, f_q, \phi^+} \mathcal{J}(f_q), \\ & \text{s.t.} \begin{cases} \|\hat{\mathbf{x}}_{t+1} - \mathbf{x}_{t+1}\| < \epsilon, \\ \hat{\mathbf{x}}_{t+1} = \phi^\dagger(f_q(\phi(\mathbf{x}_t))). \end{cases} \end{aligned} \quad (32)$$

We know that  $\hat{X}_{t+1} = \psi_\omega^{-1}(\hat{Y}_{t+1} \oplus \xi)$ , where  $\psi_\omega^{-1}$  is a reversible mapping that doesn't affect the mutual information according to Lemma 7.1. Therefore, based on Lemma 7.2, we can perform a transformation on our optimization objective  $\mathcal{J}(f_q)$ :

$$\mathcal{J}(f_q) = I(Y_t, \hat{Y}_{t+1}) = I(Y_t, \hat{X}_{t+1}). \quad (33)$$

Here,  $I$  represents mutual information. By utilizing the property of mutual information, we can derive the following equation:

$$I(Y_t, \hat{X}_{t+1}) = H(Y_t) - H(Y_t | \hat{X}_{t+1}). \quad (34)$$

Now,  $H(\tilde{Y}_t) = H(U_q)$ , where  $U_q$  is a uniform distribution on a macro space. Therefore, we have:

$$\mathcal{J}(f_{\theta,q}) = H(U_q) - H(\tilde{Y}_t | \tilde{X}_{t+1}). \quad (35)$$

The optimization of the objective function  $\mathcal{J}(f_q)$  can be reformulated as the optimization of the conditional entropy  $H(\tilde{Y}_t | \tilde{X}_{t+1})$ , since  $H(U_q)$  is a constant. The variational upper bound on  $H(\tilde{Y}_t | \tilde{X}_{t+1})$  is obtained by Lemma 7.3.

$$H(\tilde{Y}_t | \tilde{X}_{t+1}) \leq - \iint \tilde{p}(\mathbf{y}_t, \mathbf{x}_{t+1}) \ln g(\mathbf{y}_t | \mathbf{x}_{t+1}) d\mathbf{y}_t d\mathbf{x}_{t+1}, \quad (36)$$

where  $\tilde{p}$  represents the probability distribution function of random variables in case of  $\mathbf{y}_t$  being intervened.

We will use a neural network to fit the distribution  $g(\mathbf{y}_t | \mathbf{x}_{t+1})$ . Based on the assumption, we can consider it as a normal distribution. According to Lemma 7.3, since the conditional probability  $g(\mathbf{y}_t | \mathbf{x}_{t+1})$  can be any distribution, we can assume it to be a normal distribution for simplicity. Predicting  $\mathbf{y}_t$  with  $\mathbf{x}_{t+1}$  as input can be divided into two steps. First,  $\mathbf{x}_{t+1}$  is encoded by the encoder  $\phi$  into the macro latent space. Then, the reverse macro dynamics are approximated using  $g_{\theta'}$ . As a result, the expectation of  $g(\mathbf{y}_t | \mathbf{x}_{t+1})$  can be obtained using the following equation:

$$E_g(\tilde{Y}_t | X_{t+1} = \mathbf{x}_{t+1}) \equiv g_{\theta'}(\phi(\mathbf{x}_{t+1})) \quad (37)$$

Therefore, we have  $g(\mathbf{y}_t | \mathbf{x}_{t+1}) \sim N(\mu, \Sigma)$ , where  $\Sigma$  is a constant diagonal matrix and  $\mu = g_{\theta'}(\phi(\mathbf{x}_{t+1}))$ . In order to utilize the properties of intervention on  $\mathbf{y}_t$ , we need to separate  $\tilde{p}(\mathbf{y}_t)$ . Following Equation 36, we can further transform  $H(\tilde{Y}_t | \tilde{X}_{t+1})$ :

$$H(\tilde{Y}_t | \tilde{X}_{t+1}) \leq - \iint \tilde{p}(\mathbf{y}_t) \tilde{p}(\mathbf{x}_{t+1} | \mathbf{y}_t) \ln g(\mathbf{y}_t | \mathbf{x}_{t+1}) d\mathbf{y}_t d\mathbf{x}_{t+1}. \quad (38)$$

Assuming that the training is sufficient, we can have

$$\tilde{p}(\mathbf{x}_{t+1} | \mathbf{y}_t) \approx p(\mathbf{x}_{t+1} | \mathbf{y}_t). \quad (39)$$

So,

$$H(\tilde{Y}_t | \tilde{X}_{t+1}) \leq - \iint \tilde{p}(\mathbf{y}_t) p(\mathbf{x}_{t+1} | \mathbf{y}_t) \ln g(\mathbf{y}_t | \mathbf{x}_{t+1}) d\mathbf{y}_t d\mathbf{x}_{t+1}. \quad (40)$$

According to Equation 37, we obtain the logarithm probability density function of  $g(\mathbf{y}_t | \mathbf{x}_{t+1})$ :

$$\begin{aligned} \ln g(\mathbf{y}_t | \mathbf{x}_{t+1}) & \approx \ln \frac{1}{(2\pi)^{\frac{m}{2}} |\Sigma|^{\frac{1}{2}}} e^{-\frac{(\mathbf{y}_t - g_{\theta'}(\phi(\mathbf{x}_{t+1})))^2}{2|\Sigma|}} \\ & = -\frac{(\mathbf{y}_t - g_{\theta'}(\phi(\mathbf{x}_{t+1})))^2}{2|\Sigma|} + \ln \frac{1}{(2\pi)^{\frac{m}{2}} |\Sigma|^{\frac{1}{2}}}. \end{aligned} \quad (41)$$

Because  $\ln \frac{1}{(2\pi)^{\frac{m}{2}} |\Sigma|^{\frac{1}{2}}} \geq \ln \frac{1}{(2\pi)^{\frac{m}{2}} |\Sigma|^{\frac{1}{2}}_{max}}$ , so

$$\begin{aligned} H(\tilde{Y}_t | \tilde{X}_{t+1}) &\leq \iint \tilde{p}(\mathbf{y}_t) p(\mathbf{x}_{t+1} | \mathbf{y}_t) \left[ \frac{(\phi(\mathbf{x}_t) - g_{\theta'}(\phi(\mathbf{x}_{t+1})))^2}{2|\Sigma|} - \ln \frac{1}{(2\pi)^{\frac{m}{2}} |\Sigma|^{\frac{1}{2}}} \right] d\mathbf{y}_t d\mathbf{x}_{t+1} \\ &\leq \iint \tilde{p}(\mathbf{y}_t) p(\mathbf{x}_{t+1} | \mathbf{y}_t) \left[ \frac{(\phi(\mathbf{x}_t) - g_{\theta'}(\phi(\mathbf{x}_{t+1})))^2}{2|\Sigma|_{min}} - \ln \frac{1}{(2\pi)^{\frac{m}{2}} |\Sigma|^{\frac{1}{2}}_{max}} \right] d\mathbf{y}_t d\mathbf{x}_{t+1}, \end{aligned} \quad (42)$$

where  $|\Sigma|_{min} = \sigma_{min}^q$ ,  $|\Sigma|_{max} = \sigma_{max}^q$ . Here,  $\tilde{p}(\mathbf{y}_t) p(\mathbf{x}_{t+1} | \mathbf{y}_t) = \frac{\tilde{p}(\mathbf{y}_t)}{p(\mathbf{y}_t)} p(\mathbf{x}_{t+1}, \mathbf{y}_t)$ . Thus, we obtain  $\frac{\tilde{p}(\mathbf{y}_t)}{p(\mathbf{y}_t)}$ , where  $\tilde{p}(\mathbf{y}_t)$  represents the target distribution and  $p(\mathbf{y}_t)$  represents the natural distribution obtained from the data. We can define the inverse probability weights  $w(\mathbf{x}_t)$  as follows:

$$w(\mathbf{x}_t) \equiv \frac{\tilde{p}(\mathbf{y}_t)}{p(\mathbf{y}_t)}. \quad (43)$$

Let  $z = \frac{(\phi(\mathbf{x}_t) - g_{\theta'}(\phi(\mathbf{x}_{t+1})))^2}{2|\Sigma|_{min}} - \ln \frac{1}{(2\pi)^{\frac{m}{2}} |\Sigma|^{\frac{1}{2}}_{max}}$ . Therefore, we can express Equation 42 as follows:

$$H(\tilde{Y}_t | \tilde{X}_{t+1}) \leq \iint w(\mathbf{x}_t) p(\mathbf{x}_{t+1}, \mathbf{y}_t) z d\mathbf{y}_t d\mathbf{x}_{t+1}. \quad (44)$$

Because we train neural networks using discrete samples  $\{\mathbf{x}_t\}$ , we can use the sample mean as an approximate estimate of the expectation in Equation 44. Therefore, the variational upper bound of  $H(\tilde{Y}_t | \tilde{X}_{t+1})$  can be written as:

$$H(\tilde{Y}_t | \tilde{X}_{t+1}) \leq \frac{1}{T} \sum_{i=0}^{T-1} w(\mathbf{x}_t) z. \quad (45)$$

Substituting the equation into Equation 35, we obtain the variational lower bound of the original objective function:

$$\mathcal{J}(f_{\theta,q}) \geq H(U_q) - \frac{1}{T} \sum_{i=0}^{T-1} w(\mathbf{x}_t) z. \quad (46)$$

Therefore, the optimization problem (Equation 1) is transformed into

$$\min_{\omega, \theta, \theta'} \sum_{i=0}^{T-1} w(\mathbf{x}_t) |\phi(\mathbf{x}_t) - g_{\theta'}(\phi(\mathbf{x}_{t+1}))|^2 \quad (47)$$

$$s.t. ||\hat{\mathbf{x}}_{t+1} - \mathbf{x}_{t+1}|| < \epsilon, \quad (48)$$

where  $\omega$ ,  $\theta$ ,  $\theta'$  respectively represent the parameters of the three neural networks  $\psi$ ,  $f_\theta$ ,  $g_{\theta'}$  in the NIS+ framework.

Then we construct Lagrange function,

$$L(\omega, \theta, \theta', \lambda) = \sum_{i=0}^{T-1} w(\mathbf{x}_t) |\phi(\mathbf{x}_t) - g_{\theta'}(\phi(\mathbf{x}_{t+1}))|^2 + \lambda ||\phi^\dagger(\mathbf{y}_{t+1}) - \mathbf{x}_{t+1}|| \quad (49)$$

Therefore, the optimization goal is transformed into

$$\min_{\omega, \theta, \theta'} \sum_{i=0}^{T-1} w(\mathbf{x}_t) ||\mathbf{y}_t - g_{\theta'}(\mathbf{y}_{t+1})|| + \lambda ||\hat{\mathbf{x}}_{t+1} - \mathbf{x}_{t+1}|| \quad (50)$$

□

### 7.2.2. Proof of Theorem 5.2

We will first use two separate lemmas to prove the scalability of stacked encoder and parallel encoder, thereby demonstrating that their arbitrary combination can keep the conclusion of Theorem 5.1 unchanged.

**Lemma 7.4** (Mutual information will not be affected by stacked encoder). *If  $X \in \text{Dom}(X)$  and  $Y \in \text{Dom}(Y)$  form a Markov chain  $X \rightarrow Y$ , and  $\Phi_L$  and  $\Phi_L^\dagger$  represent the  $L$ -layer stacked encoder and decoder, respectively, then:*

$$I(X; Y) = I(X; \Phi_L^\dagger(Y)). \quad (51)$$

*Proof.* According to Figure 9(a), we can obtain

$$\Phi_L^\dagger(Y) = \phi_{q_1}^\dagger \circ \phi_{q_2}^\dagger \circ \dots \circ \phi_{q_L}^\dagger(Y). \quad (52)$$

$\phi_{q_i}^\dagger (i = 1, 2, \dots, L) : \mathcal{R}^{q_i} \rightarrow \mathcal{R}^{q_{i-1}}$  is a basic decoder as shown in Equation 11.  $\circ$  represents the composition of functions. Therefore, according to Lemma 7.2 and the fact that reversible mappings do not change mutual information, we obtain

$$I(X; Y) = I(X; \Phi_L^\dagger(Y)). \quad (53)$$

Let  $Y_{L-1} = \Phi_L^\dagger(Y)$ , we can further obtain  $I(X; Y_{L-1}) = I(X; \Phi_{L-1}^\dagger(Y_{L-1}))$ , and so on, leading to the final result

$$I(X; Y) = I(X; \Phi_L^\dagger(Y)). \quad (54)$$

□

**Lemma 7.5** (Mutual information will not be affected by parallel encoder). *If  $X \in \text{Dom}(X)$  and  $Y \in \text{Dom}(Y)$  form a Markov chain  $X \rightarrow Y$ , and  $\Phi_T$  and  $\Phi_T^\dagger$  represent parallel encoder and decoder composed of  $T$  ordinary encoders or decoders, respectively, then:*

$$I(X; Y) = I(X; \Phi_T^\dagger(Y)). \quad (55)$$

*Proof.* the decoding process can be divided into two steps:

$$\Phi_T^\dagger(Y) = \Psi_T(Y \bigoplus \xi). \quad (56)$$

$Y$  can be decomposed as  $Y = Y_1 \bigoplus Y_2 \bigoplus \dots \bigoplus Y_T$ , and all the introduced noise  $\xi = \xi_1 \bigoplus \xi_2 \bigoplus \dots \bigoplus \xi_T$ , even if the order of their concatenation changes, it will not affect the mutual information between the overall variable and other variables. Let  $\Psi_T(Z) = \psi_1(Z_1) \bigoplus \psi_2(Z_2) \bigoplus \dots \bigoplus \psi_T(Z_T)$ , where  $Z_i (i = 1, 2, \dots, T)$  is a partition of  $Z$ , and  $\psi_i (i = 1, 2, \dots, T) : \mathcal{R}^p \rightarrow \mathcal{R}^p$  are all invertible functions. Therefore,  $\Psi_T$  is also an invertible function, meaning that this function transformation does not change the mutual information. According to Lemma 7.2, we have

$$I(X; Y) = I(X; Y \bigoplus \xi) = I(X; \Psi_T(Y \bigoplus \xi)). \quad (57)$$

Finally proven,

$$I(X; Y) = I(X; \Phi_T^\dagger(Y)). \quad (58)$$

□

Next, we provide the proof of Theorem 5.2.

**Theorem 5.2** (Problem Transformation in Extensions of NIS+ Theorem) When the encoder of NIS+ is replaced with an arbitrary combination of stacked encodes and parallel encoders, the conclusion of Theorem 2.1 still holds true.

*Proof.* To demonstrate that Theorem 5.1 remains applicable to the extended NIS+ framework, we only need to prove that Equation 33 still holds true, as the only difference between the extended NIS+ and the previous framework lies in the encoder. First, we restate Equation 33 as follows:

$$\mathcal{J}(f_q) = I(Y_t, \hat{Y}_{t+1}) = I(Y_t, \hat{X}_{t+1}). \quad (59)$$

According to Lemma 7.4 and Lemma 7.5, Equation 33 holds true when the encoder of NIS+ is replaced with either a stacked encoder or a parallel encoder. And any combination of these two encoders is nothing more than an alternating nesting of stacking and parallelization, so the conclusion still holds. □



### 7.2.3. Proof of Theorem 5.3

To prove the universality theorem, we need to extend the definition of the basic encoder by introducing a new operation  $\eta_{p,s} : \mathcal{R}^p \rightarrow \mathcal{R}^s$ , which represents the self-replication of the original variables.

$$\eta_{p,s}(\mathbf{x}) = \mathbf{x} \oplus \mathbf{x}_{s-p}. \quad (60)$$

The vector  $\mathbf{x}_{s-p}$  is composed of  $s-p$  dimensions, where each dimension is a duplicate of a specific dimension in  $\mathbf{x}$ . For example, if  $\mathbf{x} = (0.1, 0.2, 0.3)$ , then  $\eta_{2,5}(\mathbf{x}) = (0.1, 0.2, 0.3, 0.1, 0.2)$ .

The basic idea to prove theorem 5.3 is to use the famous universal approximation theorems of common feed-forward neural networks mentioned in [52, 53] and of invertible neural networks mentioned in [54, 55] as the bridges, and then try to prove that any feed-forward neural network can be simulated by a series of bijective mapping( $\psi$ ), projection( $\chi$ ) and vector expansion ( $\eta$ ) procedures. The basic encoder after the extension for vector expansion can be expressed by the following equation:

$$\phi = Proj_q \circ \psi_s \circ \eta_{p,s} \circ \psi_p. \quad (61)$$

The functions  $\psi_s : \mathcal{R}^s \rightarrow \mathcal{R}^s$  and  $\psi_p : \mathcal{R}^p \rightarrow \mathcal{R}^p$  represent two reversible mappings. The final dimensionality  $q$  that is retained may be larger than the initial dimensionality  $p$ . In the context of coarse-graining microscopic states to obtain macroscopic states, for the sake of convenience, we usually consider  $\phi$  as a dimension reduction operator.

First, we need to prove a lemma.

**Lemma 7.6.** *For any vector  $X \in \mathcal{R}^p$  and matrix  $W \in \mathcal{R}^{s \times p}$ , where  $s, p \in \mathcal{N}$ , there exists an integer  $s_1 \leq \min(s, p)$  and two basic units of encoder:  $\psi_s \circ \eta_{s_1,s}$  and  $\chi_{p,s_1} \circ \psi_p$  such that:*

$$W \cdot X \simeq (\psi_s \circ \eta_{s_1,s}) \circ (\chi_{p,s_1} \circ \psi_p)(X), \quad (62)$$

where,  $\simeq$  represents approximate or simulate.

*Proof.* For any  $W \in \mathcal{R}^{s \times p}$ , we can SVD decomposes it as:

$$W = U \cdot \Lambda \cdot V, \quad (63)$$

where  $U \in \mathcal{R}^{s \times s}$ ,  $V \in \mathcal{R}^{p \times p}$  are all orthogonal matrices,  $\Lambda = \begin{pmatrix} diag(\lambda_1, \lambda_2, \dots, \lambda_{s_1}) & \mathbf{0} \\ \mathbf{0} & \mathbf{0} \end{pmatrix}_{s \times p}$  is a diagonal matrix composed by nonzero eigenvalues of  $W$ :  $\lambda_i, i \in [1, s_1]$ , and zeros, where  $s_1$  is the rank of the matrix  $W$ . Because all matrices can be regarded as functions, therefore:

$$W(X) = U(\eta_{s_1,s}(\chi_{p,s_1}(\Lambda' \cdot V)(X))), \quad (64)$$

where,  $\Lambda' = diag(\lambda_1, \lambda_2, \dots, \lambda_{s_1}, 1, \dots, 1)$ . That is, the functional mapping process of  $W(X)$  can be decomposed into four steps: matrix multiplication by  $\Lambda' \cdot V$ , projection  $\chi_{p,s_1}$  (projecting a  $p$  dimensional vector to an  $s_1$  dimensional vector), vector expansion  $\eta_{s_1,s}$  (expanding the  $s_1$  dimensional vector to an  $s$  dimensional one), and matrix multiplication by  $U$ . Notice that the first and the last steps are invertible because the corresponding matrices are invertible. Therefore, according to [54, 55], there are invertible neural networks  $\psi_s$  and  $\psi_p$  that can simulate orthogonal matrix  $U$  and the invertible matrix  $\Lambda' \cdot V$ , respectively. Thus,  $\psi_s \simeq U$ , and  $\psi_p \simeq \Lambda' \cdot V$ . Then we have:

$$(\psi_s \circ \eta_{s_1,s}) \circ (\chi_{p,s_1} \circ \psi_p) \simeq W, \quad (65)$$

That is  $W(X)$  can be approximated by an extended stacked encoder.  $\square$

With lemma 7.6, we can prove theorem 5.3. We at first restate theorem 5.3 here:

**Theorem 5.3**(Universal Approximating Theorem of Stacked Encoder): For any continuous function  $f$  which is defined on  $K \times \mathcal{R}^p$ , where  $K \in \mathcal{R}^p$  is a compact set, and  $p > q \in \mathcal{Z}^+$ , there exists an integer  $s$  and an extended stacked encoder  $\phi_{p,s,q} : \mathcal{R}^p \rightarrow \mathcal{R}^q$  with  $s$  hidden size and an expansion operator  $\eta_{p,s}$  such that:

$$\phi_{p,s,q} \simeq f, \quad (66)$$

Thereafter, an extended stacked encoder is of universal approximation property which means that it can approximate(simulate) any coarse-graining function defined on  $\mathcal{R}^p \times \mathcal{R}^q$ .

*Proof.* According to universal approximation theorem in [52, 53], for any function  $f$  defined on  $K \times \mathcal{R}^p$ , where  $K \in \mathcal{R}^p$  is a compact set, and  $p > q \in \mathcal{Z}^+$ , and small number  $\epsilon$ , there exists an integer  $s$  and  $W \in \mathcal{R}^{s \times p}$ ,  $W' \in \mathcal{R}^{q \times s}$ ,  $b \in \mathcal{R}^s$  such that:

$$W' \cdot \sigma(W + b) \simeq f, \quad (67)$$

where,  $\sigma(\mathbf{x}) = 1/(1 + \exp(-\mathbf{x}))$  is the sigmoid function on vectors.

According to Lemma 7.6 and  $+b$  and  $\sigma(\cdot)$  are all invertible operators, therefore, there exists invertible neural networks  $\psi_q, \psi'_s, \psi_s, \psi_p$ , and two integers  $s_1, s_2$  which are ranks of matrices  $W'$  and  $W$ , respectively, such that:

$$(\psi_q \circ \eta_{s_2, q} \circ \chi_{s, s_2} \circ \psi'_s) \circ (\psi_s \circ \eta_{s_1, s} \circ \chi_{p, s_1} \circ \psi_p) \simeq W' \cdot \sigma(W \cdot +b), \quad (68)$$

where,  $\psi_s \circ \eta_{s_1, s} \circ \chi_{p, s_1} \circ \psi_p$  approximates(simulates) the function  $\sigma(W \cdot +b)$  and  $\psi_q \circ \eta_{s_2, q} \circ \chi_{s, s_2} \circ \psi'_s$  approximates(simulates) the function  $W'$ .

Therefore, if we let  $\phi_{p, s, q} = (\psi_q \circ \eta_{s_2, q} \circ \chi_{s, s_2} \circ \psi'_s) \circ (\psi_s \circ \eta_{s_1, s} \circ \chi_{p, s_1} \circ \psi_p)$ , then  $\phi_{p, s, q} \simeq f$   $\square$

In real applications, although the basic encoder and the extended versions do not include expansion operator, we always expand input vector before it is input for the encoder. Therefore, it is reasonable to believe that Theorem 5.3 still holds for stacked encoders.

### 7.3. SIR Model

In this section, we will introduce various parameters for generating data in the SIR experiment. In Equation 6,  $\xi_1, \xi_2 \sim N(0, \Sigma)$  are two-dimensional Gaussian noises and independent each other, and  $\Sigma = \begin{pmatrix} \sigma & -\frac{1}{2}\sigma \\ -\frac{1}{2}\sigma & \sigma \end{pmatrix}$ . For this covariance matrix, we can easily deduce that  $\xi_1$  and  $\xi_2$  are both two-dimensional normal distributions with a correlation coefficient of  $-\frac{1}{2}$ . The parameter  $\sigma$  controls the overall magnitude of the noise, which is set to  $\sigma = 0.03$  in the experiments conducted in this paper. For macroscopic state data, we discretize the original continuous model with  $dt = 0.01$  and run 7 time steps for each starting point. After sampling with different starting points, we concatenate equal amounts of  $\xi_1$  and  $\xi_2$  to obtain four-dimensional microscopic data.

In the SIR model experiment conducted in this article, we generated two datasets: the complete dataset and the partial dataset. For the complete dataset, we uniformly sampled 9000 initial points from the entire range of possible values for  $S$  and  $I$  ( $S \geq 0, I \geq 0, S+I \leq 1$ ), resulting in a total of 63000 data points. For the partial dataset, we uniformly sampled 6000 initial points from the region where  $S \geq \frac{1}{3}$ . Additionally, to satisfy the requirements of KDE estimation for the support set, we randomly sampled 10 initial points from the region where  $S \leq \frac{1}{3}$ . In total, the partial dataset consists of 42070 sample points. The training and testing results of the NIS+ neural network on these two different sample sets are presented in Figure 3.

To compare the advantages of the NIS+ framework itself, we constructed a regular fully connected neural network(NN) with 33,668 parameters, and a NIS+ framework with a similar number of parameters in the SIR experiment (a total of 37,404 parameters including the inverse dynamics). NN consists of an input layer, an output layer, and four hidden layers with 4, 64, 128, 128, 64, 4 neurons respectively. Reweighted-NN refers to the NN that combines inverse probability weighting technique, with the same parameter framework. For each data point  $\mathbf{x}_t$ , we estimate the KDE probability distribution and calculate the inverse probability weighting. Finally, the weights are multiplied with the loss to give different training weights to samples with different densities. The comparison results are shown in Figure 3.

We also draw Figure 11 to show the comparison of the vector fields between the emergent dynamics and the real SIR dynamics without normalization operation. It is clear that the one to one correspondence still exists, but the angles are different from the ones in Figure 3(d).

### 7.4. Boids Model

In 1986, Craig Reynolds created a simulation of the collective behavior of birds, known as the Boids model [39]. This model only used three simple rules to control the interactions between individuals, resulting in flock-like behavior.

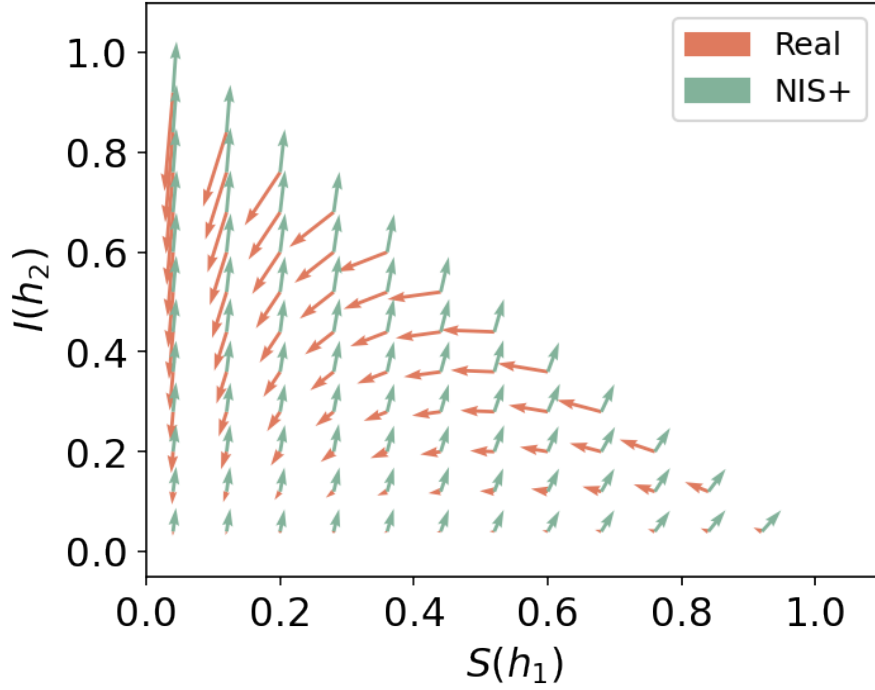


**Figure 11.** Vector field (without normalization) comparison between the emergent dynamics learned by NIS+ and the true dynamics of the SIR model. The arrows represent the direction and magnitude of the dynamics' derivatives on the domain. It can be observed that there exists a fixed angular relationship between the derivatives of the emergent dynamics learned by NIS+ and the true dynamics. For ease of presentation, the arrows corresponding to the derivatives of the emergent dynamics are magnified 20 times to account for the inconsistency in data ranges between the latent space and the SIR phase space.

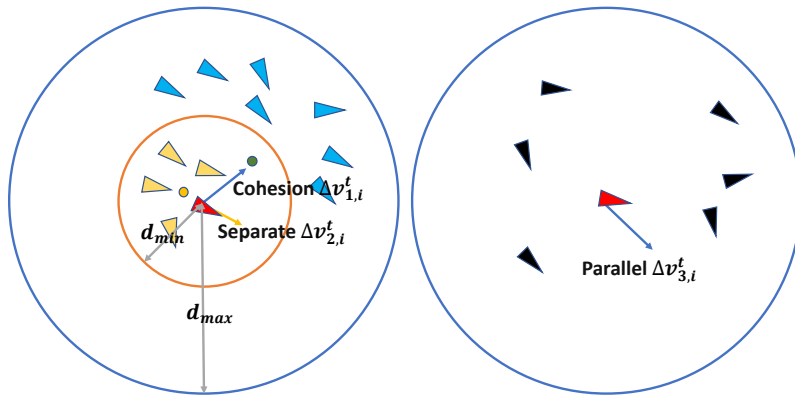


**Figure 12. Boids model.** By modifying  $d_{\max}$  and  $d_{\min}$  at time  $t$ , the aggregation of bird flocks will change. Specify  $\Delta v_{1,i}^t$ ,  $\Delta v_{2,i}^t$ ,  $\Delta v_{3,i}^t$  as the variation of separation, parallelism, and cohesion velocities, respectively. The  $i$ -th bird is marked in red. At time  $t$ , birds with a distance less than  $d_{\min}$  from bird  $i$  will affect  $\Delta v_{2,i}^t$ . Birds with a distance less than  $d_{\max}$  from bird  $i$  will affect  $\Delta v_{1,i}^t$ ,  $\Delta v_{3,i}^t$ . In this way, birds can maintain a distance from each other and allow the Boids to fly in an orderly manner in one direction.

#### 7.4.1. Method of Simulating the Trajectory of Boids

The motion vector of bird  $i$  at time  $t$  can be expressed as  $(x_i^t, y_i^t, v_{x,i}^t, v_{y,i}^t)$  where  $x_i^t$  and  $y_i^t$  represent the position coordinates,  $v_{x,i}^t$  and  $v_{y,i}^t$  represent the projection of velocity on two coordinate axes. With  $N$  boids,  $i = 1, 2, \dots, N$ . The motion vector can be decomposed into position vector and velocity vector  $\mathbf{x}_i^t = (x_i^t, y_i^t)$  and  $\mathbf{v}_i^t = (v_{x,i}^t, v_{y,i}^t)$ . The distance between two boids  $i$  and  $j$  can be expressed as  $d_{ij} = \|\mathbf{x}_i^t - \mathbf{x}_j^t\| = \sqrt{(x_i - x_j)^2 + (y_i - y_j)^2}$ . Although the Boids model belongs to a continuous system, in order to facilitate the simulation process and subsequent experiments, we uniformly set  $\Delta t = 1$ . For a single boid in the model, the acceleration  $\mathbf{a}_i^t = \mathbf{v}_i^{t+1} - \mathbf{v}_i^t$  can be divided into four parts: separation, parallelism, cohesion, and random deflection angle noise. We stipulate that the velocity magnitude of a boid during the flight remains stable, so the impact of acceleration mainly changes the direction of Boids' flight. After knowing the motion state vector of each boid in the flock at time  $t$ , the motion state at time  $t+1$  can be generated. Specify  $\Delta v_{1,i}^t$ ,  $\Delta v_{2,i}^t$ ,  $\Delta v_{3,i}^t$  as the variation of separation, parallelism, and cohesion velocities, respectively. In which

$$\begin{cases} \Delta v_{1,i}^t = \frac{\mathbf{x}_i^t - \mathbf{x}_{\Phi_i}^t}{\|\mathbf{x}_i^t - \mathbf{x}_{\Phi_i}^t\|}, \\ \Delta v_{2,i}^t = \frac{\sum_{k \in \Psi_i^t} \mathbf{v}_k^t}{\|\sum_{k \in \Psi_i^t} \mathbf{v}_k^t\|}, \\ \Delta v_{3,i}^t = -\frac{\mathbf{x}_i^t - \mathbf{x}_{\Psi_i}^t}{\|\mathbf{x}_i^t - \mathbf{x}_{\Psi_i}^t\|}. \end{cases} \quad (69)$$

We stipulate that the maximum and minimum detection distances for Boids are  $d_{\max}$  and  $d_{\min}$ . The sets of Boids within the minimum and maximum detection range are specified as  $\Phi_i^t = \{j | d_{ij}^t < d_{\min}\}$  and  $\Psi_i^t = \{j | d_{ij}^t < d_{\max}\}$ . So the centers of gravity of  $\Phi_i$  and  $\Psi_i$  are represented as  $\mathbf{x}_{\Phi_i}^t = \sum_{k \in \Phi_i^t} \mathbf{x}_k^t / |\Phi_i|$  and  $\mathbf{x}_{\Psi_i}^t = \sum_{k \in \Psi_i^t} \mathbf{x}_k^t / |\Psi_i|$ , which are the mean values of the boids' position coordinates within two sets. With equation

$$\Delta \mathbf{v}_i^t = \Delta v_{1,i}^t + \Delta v_{2,i}^t + \Delta v_{3,i}^t \quad (70)$$

we can obtain Equation 7 in Section 3.2. The relationship between the above variables is shown in Fig.12. By modifying the starting vector  $(x_i^0, y_i^0, v_{x,i}^0, v_{y,i}^0)$  or  $d_{\max}$  and  $d_{\min}$ , the aggregation of bird flocks will change. And we can adjust the trajectory and randomness of Boids by modifying the mean and variance of the deflection angle  $\varepsilon_i^t$  in Equation 7.

#### 7.4.2. Methods for Collecting Experimental Data and Training

We record the velocity vector and position vector of each bird at each time  $t$  during its flight as data. For each time step  $t$ , we need to record the data at that time and the data at the next time step  $t+1$ . We merge the data into  $4N$  dimensional vectors at each time step  $t$  as

$$X_t = (x_1^t, y_1^t, v_{x,1}^t, v_{y,1}^t, \dots, x_N^t, y_N^t, v_{x,N}^t, v_{y,N}^t). \quad (71)$$

This vector corresponds to our micro-state data  $X_t$ ,  $p = 64$ . We can repeat the preparation and recording stages multiple times until the data volume meets our expectations. The ID of birds is 1, 2, ..., 16, evenly divided into two sets,  $\{1, 2, \dots, 8\}$  and  $\{9, 10, \dots, 16\}$ . The model we generated contains two sets of birds randomly generated near the center of the canvas.

We generate observation data in two phases: preparation and recording. In the preparation phase, one group of birds is randomly generated within a circle with (148, 150) as the center and 5 as the radius and the other group of birds is randomly generated within a circle with (152, 150) as the center and 5 as the radius. Then by modifying the  $(v_{x,i}^0, v_{y,i}^0)$  or the mean and variance of the deflection angle  $\varepsilon_i^t$  two groups of birds can fly different trajectories in Fig.4a, 4b and 4c. The norm of the velocity vector is always 1, that is  $\|\mathbf{v}_i^t\| \equiv 1, t = 1, 2, \dots$ . We set  $d_{\max} = 5$  and  $d_{\min} = 1$  so that the birds within the same group will interact with each other, while the effects between birds in different groups can be ignored. Subsequently, we allowed two groups of birds to fly for 20 steps without affecting each other, resulting in two groups of birds with distance and relatively stable internal stability. Then the positions and velocities of all birds serve as the starting point for us to record data.

In the recording phase, we have the birds continue to run 50 steps on the basis of the preparation phase, recording the velocity and position vectors of each bird separately. We randomly sort the generated data and input them into our NIS+ model for training, using the multistory structure of the NIS+ in Fig.9 during the training process. We sample the data

for 4 batches. After inputting  $X_t$ , the microstate  $Y_t$ ,  $Y_{t+1}$  and predicted value  $\hat{X}_{t+1}$  can be output, and training can begin. The encoders and decoders are stacked, and the dynamics learners in different layers,  $q = 64, 32, 16, 8, 4, 2, 1$ , operate in parallel. This design facilitates simultaneous training for different dynamics learners with distinct dimensions and enables parallel searching for the optimal dimension, which is  $q = 8$ . Due to the previous experiments showing that the model performs better when  $q = 8$  than other scales, and having too many layers can also slow down learning efficiency, we can discard layers with  $q < 8$  in the later experiments.

After training with 800,000 epochs by NIS,  $\mathcal{J}_q$  reaches its maximum value when  $q = 8$ . We continue to optimize the existing model using NIS+ training 400,000 epochs, the results are shown in Fig.4e. Then we can obtain multi-step prediction data as shown in Figure 4a. It can be seen that the multi-step predicted trajectory matches the flight trajectory of the real bird flock. However, if the variance of  $\varepsilon_i^t$  is large, the training effect of the model will deteriorate, and the multi-step prediction distance will become shorter as shown in 4b. With the method of generating data, we can observe the impact of noise. For different observation noises, in cases where the noise is not too significant, we can use the same method to train the model with NIS first, then optimize it with NIS+ to obtain Fig.4f. For different deflection angle noises, after training from random initial parameter values, in order to unify the control variables, we optimized them in the dimension of  $q = 8$  and obtained Fig.4g.

## 7.5. Game of Life

### 7.5.1. Data generation

In this paper, we use Conway’s Game of Life as the experimental object, in which each cell has two states for two-dimensional state input: alive (1) or dead (0), and each cell is affected by its eight neighbors. The evolution of the Game of Life is only affected by the input state and its update rules, in which the Game of Life has four evolutionary rules, respectively corresponding to cell reproduction and death, and so on. The update rules for the Game of Life are shown in the following table:

**Table 1.** The update rules for the Game of Life.

$x_t$	$x_{t+1}$
0	1 (there are three living cells around)
1	0 (less than two surviving cells around the cell (excluding two))
	1 (there are two or three living cells around)
	0 (there are more than three living cells around)

The training sample generation process of the Game of Life is as follows: firstly, a state  $x_t$  is initialized. When considering a temporal coarse-grained of two steps, the subsequent three steps of states  $x_{t+1}$ ,  $x_{t+2}$ , and  $x_{t+3}$  are then generated based on the update rule and are input to the machine learning model. The two input states are  $x_t$  and  $x_{t+1}$ , with the micro-dynamics output being  $x_{t+1}$  and  $x_{t+2}$ . Due to the utilization of spatiotemporal coarse-graining, the macro-dynamics will output a macro-state which will be decoded into the micro-states  $x_{t+2}$  and  $x_{t+3}$ . This process is repeated multiple times (50,000 samples) and generate the data for training. While in the experiments in Figure 13d and e we generate 500,000 samples.

### 7.5.2. More experiments on model ability for generalization

We then test the capability of capturing dynamical patterns on different test environments (on different space size and initial conditions), the results are shown in Figure 13a and b, respectively. The original training model has an input state size of  $18 \times 18 \times 2$  and consists of two gliders. On the basis of this model, two out-of-distribution generalization tests are carried out, as follows: (a) The out-of-distribution test of space size is performed by changing the test input state to a larger spatial scale ( $24 \times 24 \times 2$ ); (b) A generalization test involving the number of gliders was carried out, converting the original input of 2 gliders to 3 gliders. Through experimental comparison, it is found that the dynamic pattern can be captured by the model in both cases. Further, we compared the AUC of single-step predictions on micro-states for NIS and NIS+ in different initial states. As shown in Figure 13e, we found that for twenty different initial states, the method NIS+ was superior to NIS in most cases, once again verifying that the improved NIS+ method had better generalization ability.

### 7.5.3. More experiments on coarse-graining scales

In addition, we conducted a comparison of causal emergence on more scales, as shown in Figure 13c, where the size of state input is  $18 \times 18 \times 4$ , and each step state contains two gliders. By building a model as shown in Figure 5a, we can obtain three different scales. It includes one micro scale and two macro scales, in which the sizes of two macro states are respectively  $6 \times 6 \times 2$  (Macro1) and  $2 \times 2 \times 1$  (Macro2). Experimental comparison shows that the causal emergence under Macro2 scale is the most significant. Therefore, the causality of macroscopic dynamics at corresponding scales is also stronger.

Meanwhile, we also made an experimental comparison on coarse graining scale, as shown in Figure 13d. We made a comparison on different spatial sizes, including  $2 \times 2$ ,  $3 \times 3$  and  $6 \times 6$ . The result showed that  $\Delta\mathcal{J}(\text{space\_coarse } (6 \times 6)) > \Delta\mathcal{J}(\text{space\_coarse } (3 \times 3)) > \Delta\mathcal{J}(\text{space\_coarse } (2 \times 2))$ , but under the spatial division of  $6 \times 6$ , the prediction error of the model does not meet the constraints of our objective function. Therefore, the spatial scale division of  $3 \times 3$  is a better choice. Besides, we also compare two time steps and four time steps, two different time coarse-grained partitioning methods. We find that for the division of four time steps,  $\Delta\mathcal{J}$  becomes negative, and the model shows causal reduction. Therefore, the partition of space  $3 \times 3$  and the compression of 2 time steps are a better choice of parameters.

In addition, please refer to Table 2 for more detailed information on the other model parameters.

### 7.6. AAL Results

We repeat what we have done in sections 3.4 and 5.6 expect that we have utilized AAL3 atlas and made  $\lambda$  to be 0.5 for layer 1 training of NIS+ since  $\lambda = 1$  will lead to a trivial solution where macro predictions for all areas will remain the same, which make the prediction can't be meaningful. We can see a converging evidence that NIS+ framework will lead to an improvement of  $\Delta\mathcal{J}$  (see Figure 14(b)) and a stronger correlation with those areas which responds to the visual areas (See Figure 14(a) and (c)).

### 7.7. The Structure and parameters of neural networks.

Next, we list the neural network parameters used in our experimental study, as shown in Table 2. The parameter  $\lambda$  in the table is derived from Equation 12 and serves as the weight coefficient for the forward prediction error.  $L$  is an assumption about the range of data distribution, which represents the length of a hypercube with side length  $2L$  that is used to calculate the probability value for a uniform distribution. It is not difficult to see that different types of neural networks have been used to handle different types of complex systems. Both the Boids and fMRI experiments employ the Multistory NIS+ framework, which traverses different macroscopic scales and eventually selects an optimal scale (the dimension of input or output in the Inverse Dynamics Learner table).

## References

- [1] H. Sayama, *Introduction to the modeling and analysis of complex systems*. Open SUNY Textbooks, 2015.
- [2] J. Odell, "Agents and complex systems," *Journal of Object Technology*, vol. 1, no. 2, pp. 35–45, 2002.
- [3] W.-X. Wang, Y.-C. Lai, and C. Grebogi, "Data based identification and prediction of nonlinear and complex dynamical systems," *Physics Reports*, p. 1–76, Jul 2016. [Online]. Available: <http://dx.doi.org/10.1016/j.physrep.2016.06.004>
- [4] T. Kipf, E. Fetaya, K.-C. Wang, M. Welling, and R. Zemel, "Neural relational inference for interacting systems," in *International conference on machine learning*. PMLR, 2018, pp. 2688–2697.
- [5] J. Casadiego, M. Nitzan, S. Hallerberg, and M. Timme, "Model-free inference of direct network interactions from nonlinear collective dynamics," *Nature Communications*, vol. 8, no. 1, Dec 2017. [Online]. Available: <http://dx.doi.org/10.1038/s41467-017-02288-4>
- [6] Y. Zhang, Y. Guo, Z. Zhang, M. Chen, S. Wang, and J. Zhang, "Universal framework for reconstructing complex networks and node dynamics from discrete or continuous dynamics data," *Physical Review E*, vol. 106, no. 3, p. 034315, 2022.
- [7] J. H. Holland, *Emergence: From chaos to order*. OUP Oxford, 2000.



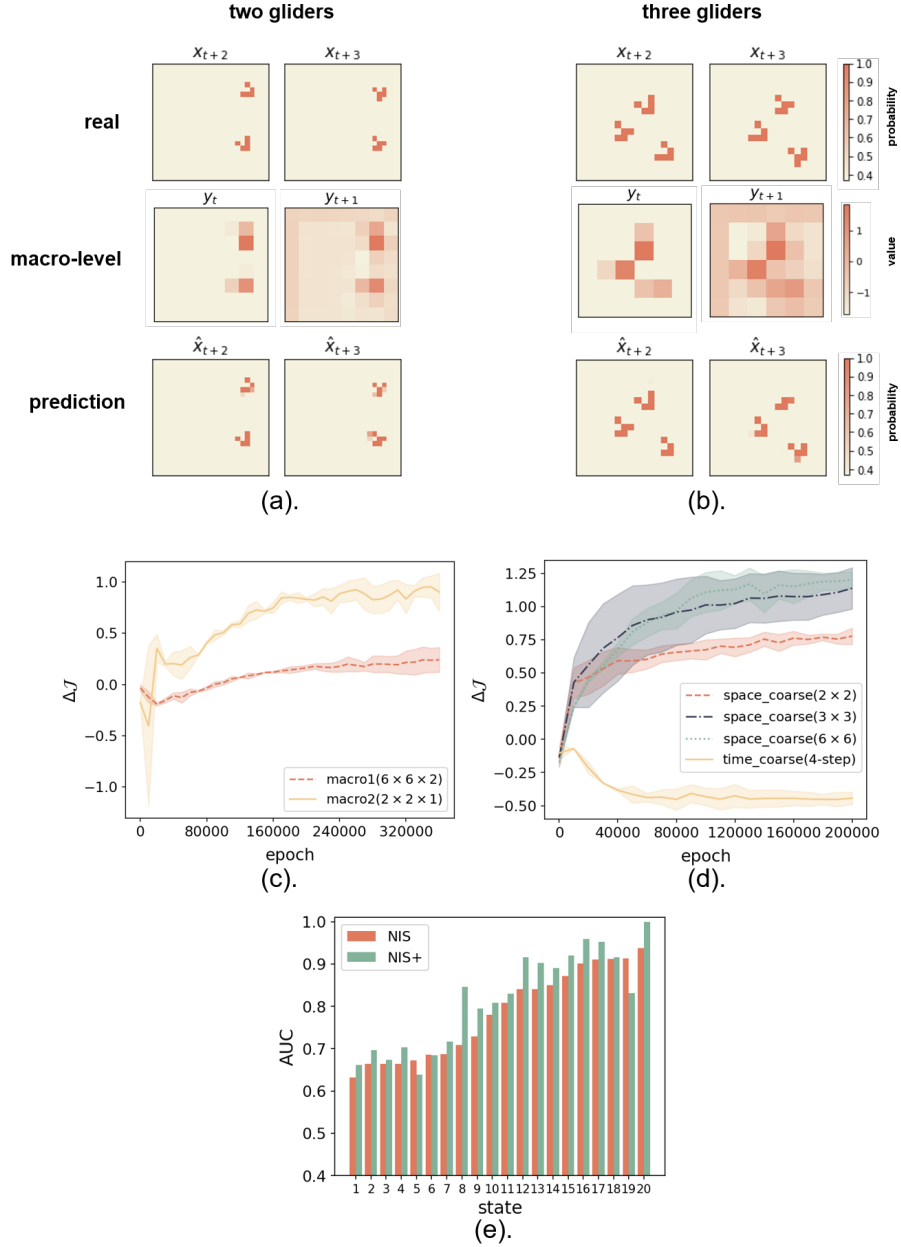


**Figure 13. Experiments of Game of Life.** (a-b) Out-of-distribution generalization test. The original training model is designed for the scenario where the input state size is  $18 \times 18 \times 2$  and consists of two gliders. Building upon this model, two out-of-distribution generalization tests were conducted as follows: (a) A spatial generalization test was performed by altering the test input to a larger spatial scale ( $24 \times 24 \times 2$ ); (b) A generalization test involving the number of gliders was conducted, transitioning from the original input of two gliders to three gliders. (c) Comparison of causal emergence at different scales. By constructing a Multistory model, we can achieve three distinct scales: one at the micro level and two at the macro level. Specifically, the two macro states have dimensions of  $6 \times 6 \times 2$  for Macro1 and  $2 \times 2 \times 1$  for Macro2, respectively. (d) Comparison of spatiotemporal coarsening scale divisions. Regarding the spatial scale division, we explore three different cases:  $2 \times 2$ ,  $3 \times 3$ , and  $6 \times 6$ . Additionally, for time coarsening, we consider compressing two time steps or four time steps into one state. In Figure 13c and d, each data point corresponds to the average of three independent runs, and the shaded area represents the standard deviation. (e) Comparison of the AUC between NIS and NIS+ based on different initial states. For the training stage, states with different patterns are selected as training samples. In the test stage, twenty states with patterns are randomly selected for testing.

**Table 2.** Parameter table for all experiments conducted using neural networks.

Experiment	Module	Parameter
SIR	Encoder(Decoder)	Three RealNVP modules Input(Onput) dimensions: 4 Macro-state dimensions: 2
	Dynamics Learner	Input(Onput) dimensions: 2 Hidden Layers: 2 Hidden Units: 64 Activation Function: LeakyReLu Total Epochs:30000 Batch Size:700 L: 1
	Inverse Dynamics Learner	$\lambda$ : 3.3 Input(Onput) dimensions: 2 Hidden Layers: 2 Hidden Units: 64 Activation Function: LeakyReLu Stage II Epochs:27000
Boids	Encoder(Decoder)	Three RealNVP modules Input(Onput) dimensions: 64 Macro-state dimensions: 32,16,8
	Dynamics Learner	Input(Onput) dimensions: 64,32,16,8 Hidden Layers: 2 Hidden Units: 32 Activation Function: LeakyReLu Total Epochs:800,000 Batch Size:4 L: 100
	Inverse Dynamics Learner	$\lambda$ : 1 Input(Onput) dimensions: 8 Hidden Layers: 2 Hidden Units: 32 Activation Function: LeakyReLu Stage II Epochs:400,000
Game of life	Encoder(Decoder)	Three RealNVP modules Input(Onput) dimensions: $18 \times 18 \times 2$ Macro-state dimensions: $6 \times 6 \times 1$
	Dynamics Learner	Input(Onput) dimensions: $6 \times 6 \times 1$ Three 2d-CNNs: (1) kernel: $3 \times 3 \times 8$ , stride 1, padding 1 Activation Function: LayerNorm, LeakyReLu; (2) kernel: $3 \times 3 \times 16$ , stride 1, padding 1 Activation Function: LayerNorm, LeakyReLu; (3) kernel: $3 \times 3 \times 1$ , stride 1, padding 1 Epochs:200000 Batch Size:50 L: 100
	Inverse Dynamics Learner	$\lambda$ : 1 Input(Onput) dimensions: $6 \times 6 \times 1$ Three 2d-CNNs: (1) kernel: $3 \times 3 \times 8$ , step 1, padding 1 Activation Function: LayerNorm, LeakyReLu; (2) kernel: $3 \times 3 \times 16$ , step 1, padding 1 Activation Function: LayerNorm, LeakyReLu; (3) kernel: $3 \times 3 \times 1$ , step 1, padding 1 Epochs:200000
fMRI	Encoder(Decoder)	Six RealNVP modules Input(Onput) dimensions: 100 Macro-state dimensions: 52,27,14,7,3,1
	Dynamics Learner	Input(Onput) dimensions: 100,52,27,14,7,3,1 Hidden Layers: 5 Hidden Units: 256 Activation Function: LeakyReLu and a final tanh Total Epochs: 60000 Batch Size: 100 L: 1
	Inverse Dynamics Learner	$\lambda$ : 1 Input(Onput) dimensions: 1 Hidden Layers: 5 Hidden Units: 256 Activation Function: LeakyReLu Stage II Epochs: 10000

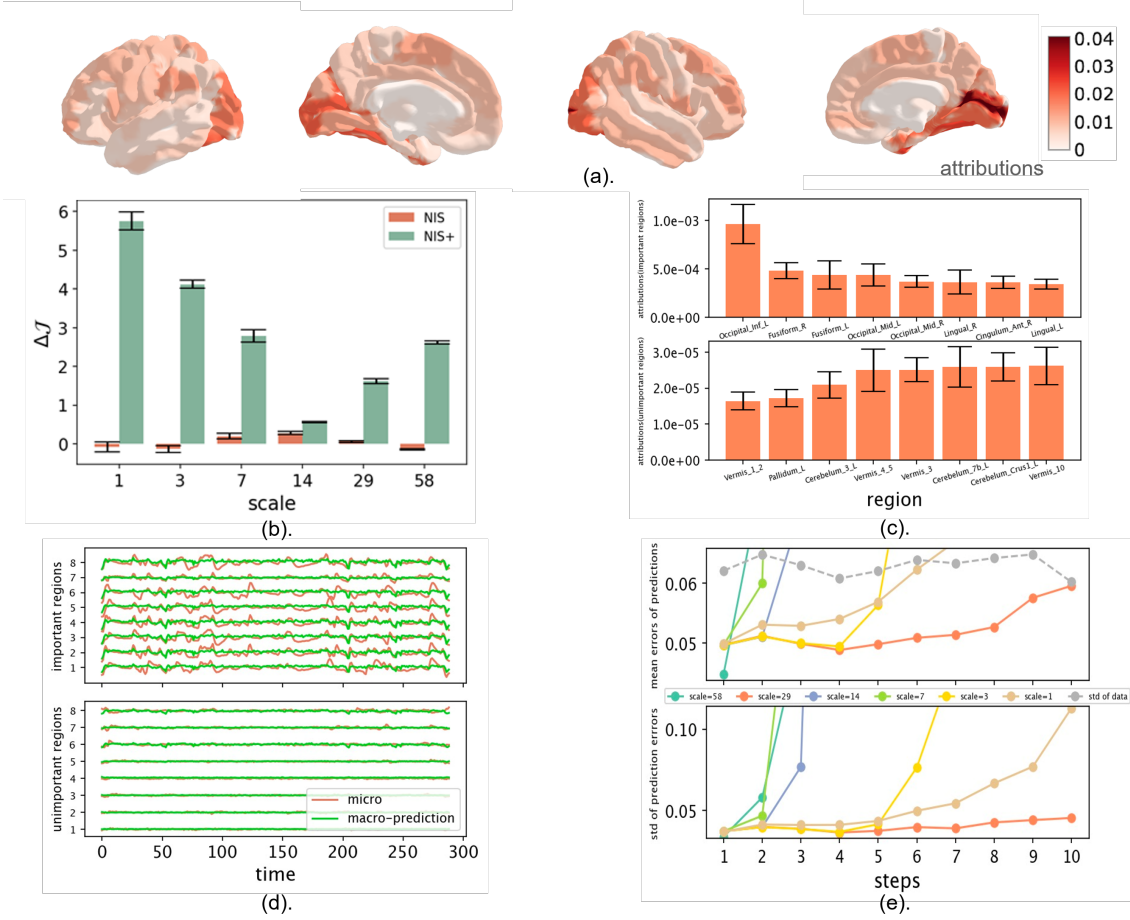


**Figure 14.** The learning results of fMRI data for the brains and the attribution analysis for the learned macro-state are presented. (a) Attribution maps, calculated using integrated gradient analysis of the encoder from the micro- to macro-scale with a scale of  $q = 1$ , are displayed. The maps show the left hemisphere from the view of the left, left hemisphere from the view of the right, right hemisphere from the view of the right, and right hemisphere from the view of the left. The colors represent the normalized absolute values of the integrated gradient. (b) Measures of causal emergence (dimension averaged) are compared among different models. It is evident that the NIS+ framework exhibits a substantial improvement in  $\Delta J$ . The error bar represents the standard deviation. (c) The attributions of top 8 significant and insignificant areas under the AAL Atlas are presented. The error bar represents the standard errors. (d) The time series visualization of the top and lowest 8 regions based on the attribution values (integrated gradient) is shown. (e) The mean errors of the multi-step predictions increase with the prediction steps under different scales ( $q$ ) on the test dataset. The grey dotted line represents the standard deviation of the data for comparison. The standard deviation of the prediction errors is also displayed below.

- [8] S. Ben Tahar, J. J. Muñoz, S. J. Shefelbine, and E. Comellas, “Turing pattern prediction in three-dimensional domains: the role of initial conditions and growth,” *bioRxiv*, pp. 2023–03, 2023.
- [9] P. C. Matthews and S. H. Strogatz, “Phase diagram for the collective behavior of limit-cycle oscillators,” *Physical Review Letters*, vol. 65, no. 14, p. 1701–1704, Jul 2002. [Online]. Available: <http://dx.doi.org/10.1103/physrevlett.65.1701>
- [10] Y. Du, Z. He, Q. Gao, H. Zhang, C. Zeng, D. Mao, and J. Zhao, “Emergent phenomena of vector solitons induced by the linear coupling,” *Laser & Photonics Reviews*, p. 2300076, 2023.
- [11] F. E. Rosas, P. A. M. Mediano, H. J. Jensen, A. K. Seth, A. B. Barrett, R. L. Carhart-Harris, and D. Bor, “Reconciling emergences: An information-

- theoretic approach to identify causal emergence in multivariate data,” *PLOS Computational Biology*, vol. 16, no. 12, p. e1008289, Dec 2020. [Online]. Available: <http://dx.doi.org/10.1371/journal.pcbi.1008289>
- [12] J. Zhang and K. Liu, “Neural information squeezer for causal emergence,” *Entropy*, vol. 25, no. 1, p. 26, 2022.
  - [13] E. O’toole, V. Nallur, and S. Clarke, “Decentralised detection of emergence in complex adaptive systems,” *ACM Transactions on Autonomous and Adaptive Systems*, vol. 12, no. 1, p. 1–31, Mar 2017. [Online]. Available: <http://dx.doi.org/10.1145/3019597>
  - [14] F. P. Kemeth, T. Bertalan, T. Thiem, F. Dietrich, S. J. Moon, C. R. Laing, and I. G. Kevrekidis, “Learning emergent partial differential equations in a learned emergent space,” *Nature communications*, vol. 13, no. 1, p. 3318, 2022.
  - [15] F. Keijzer, “Artificial life xi: Proceedings of the eleventh international conference on the simulation and synthesis of living systems,” *MIT Press eBooks*, Jan 2008.
  - [16] C. Shalizi and C. Moore, “What is a macrostate? subjective observations and objective dynamics,” *arXiv: Statistical Mechanics*, Mar 2003.
  - [17] E. P. Hoel, L. Albantakis, and G. Tononi, “Quantifying causal emergence shows that macro can beat micro,” *Proceedings of the National Academy of Sciences*, vol. 110, no. 49, pp. 19 790–19 795, 2013.
  - [18] E. P. Hoel, “When the map is better than the territory,” *Entropy*, vol. 19, no. 5, p. 188, 2017.
  - [19] J. Fromm, “Types and forms of emergence,” *arXiv: Adaptation and Self-Organizing Systems*, Jun 2005.
  - [20] G. Tononi and O. Sporns, “Measuring information integration,” *BMC neuroscience*, vol. 4, pp. 1–20, 2003.
  - [21] R. Comolatti and E. Hoel, “Causal emergence is widespread across measures of causation,” *arXiv preprint arXiv:2202.01854*, 2022.
  - [22] R. Griebenow, B. Klein, and E. Hoel, “Finding the right scale of a network: Efficient identification of causal emergence through spectral clustering,” *arXiv: Social and Information Networks*, Aug 2019.
  - [23] E. Hoel and M. Levin, “Emergence of informative higher scales in biological systems: a computational toolkit for optimal prediction and control,” *Communicative & Integrative Biology*, vol. 13, no. 1, p. 108–118, Jan 2020. [Online]. Available: <http://dx.doi.org/10.1080/19420889.2020.1802914>
  - [24] S. Marrow, E. J. Michaud, and E. Hoel, “Examining the causal structures of deep neural networks using information theory,” *Entropy*, p. 1429, Dec 2020. [Online]. Available: <http://dx.doi.org/10.3390/e22121429>
  - [25] P. R. Vlachas, G. Arampatzis, C. Uhler, and P. Koumoutsakos, “Multiscale simulations of complex systems by learning their effective dynamics,” *Nature Machine Intelligence*, vol. 4, no. 4, pp. 359–366, 2022.
  - [26] D. Floryan and M. D. Graham, “Data-driven discovery of intrinsic dynamics,” *Nature Machine Intelligence*, vol. 4, no. 12, pp. 1113–1120, 2022.
  - [27] L. Cai and S. Ji, “A multi-scale approach for graph link prediction,” *Proceedings of the AAAI Conference on Artificial Intelligence*, p. 3308–3315, Jun 2020. [Online]. Available: <http://dx.doi.org/10.1609/aaai.v34i04.5731>
  - [28] Z. Chen, S. Li, B. Yang, Q. Li, and H. Liu, “Multi-scale spatial temporal graph convolutional network for skeleton-based action recognition,” *Proceedings of the AAAI Conference on Artificial Intelligence*, p. 1113–1122, Sep 2022. [Online]. Available: <http://dx.doi.org/10.1609/aaai.v35i2.16197>
  - [29] D. Hafner, T. Lillicrap, M. Norouzi, and J. Ba, “Mastering atari with discrete world models,” *arXiv: Learning*, Oct 2020.
  - [30] Y. LeCun, “A path towards autonomous machine intelligence version 0.9. 2, 2022-06-27,” *Open Review*, vol. 62, 2022.
  - [31] L. R. Goldberg, “The book of why: The new science of cause and effect,” *Notices of the American Mathematical Society*, p. 1, Aug 2019. [Online]. Available: <http://dx.doi.org/10.1090/noti1912>

- [32] Z. Shen, J. Liu, Y. He, X. Zhang, R. Xu, H. Yu, and P. Cui, “Towards out-of-distribution generalization: A survey,” *Cornell University - arXiv, Cornell University - arXiv*, Aug 2021.
- [33] B. Schölkopf and J. von Kügelgen, “From statistical to causal learning,” *arXiv preprint arXiv:2204.00607*, 2022.
- [34] D. Janzing, J. Peters, E. Sgouritsa, K. Zhang, J. Mooij, and B. Ickhof, “On causal and anticausal learning,” *International Conference on Machine Learning*, Jun 2012.
- [35] W. O. Kermack and A. G. McKendrick, “A contribution to the mathematical theory of epidemics,” *Proceedings of the royal society of london. Series A, Containing papers of a mathematical and physical character*, vol. 115, no. 772, pp. 700–721, 1927.
- [36] A. Attanasi, A. Cavagna, L. Del Castello, I. Giardina, T. S. Grigera, A. Jelić, S. Melillo, L. Parisi, O. Pohl, E. Shen *et al.*, “Information transfer and behavioural inertia in starling flocks,” *Nature physics*, vol. 10, no. 9, pp. 691–696, 2014.
- [37] M. Gardner, “The fantastic combinations of john conway’s new solitaire game ‘life,’” *Sc. Am.*, vol. 223, pp. 20–123, 1970.
- [38] M. Rosenblatt, “Remarks on some nonparametric estimates of a density function,” *The annals of mathematical statistics*, pp. 832–837, 1956.
- [39] C. W. Reynolds, “Flocks, herds and schools: A distributed behavioral model,” in *Proceedings of the 14th annual conference on Computer graphics and interactive techniques*, 1987, pp. 25–34.
- [40] C. W. Reynolds *et al.*, “Steering behaviors for autonomous characters,” in *Game developers conference*, vol. 1999. Citeseer, 1999, pp. 763–782.
- [41] M. Sundararajan, A. Taly, and Q. Yan, “Axiomatic attribution for deep networks,” *CoRR*, vol. abs/1703.01365, 2017. [Online]. Available: <http://arxiv.org/abs/1703.01365>
- [42] L. Snoek, M. van der Miesen, T. Beemsterboer, A. Leij, A. Eigenhuis, and H. Scholte, “The amsterdam open mri collection, a set of multimodal mri datasets for individual difference analyses,” *Scientific Data*, vol. 8, 03 2021.
- [43] A. Schaefer, R. Kong, E. M. Gordon, T. O. Laumann, X.-N. Zuo, A. J. Holmes, S. B. Eickhoff, and B. T. T. Yeo, “Local-Global Parcellation of the Human Cerebral Cortex from Intrinsic Functional Connectivity MRI,” *Cerebral Cortex*, vol. 28, no. 9, pp. 3095–3114, 07 2017. [Online]. Available: <https://doi.org/10.1093/cercor/bhx179>
- [44] L. Dinh, J. Sohl-Dickstein, and S. Bengio, “Density estimation using real nvp,” *International Conference on Learning Representations, International Conference on Learning Representations*, May 2016.
- [45] M. Sundararajan, A. Taly, and Q. Yan, “Axiomatic attribution for deep networks,” *Cornell University - arXiv, Cornell University - arXiv*, Mar 2017.
- [46] O. Esteban, C. Markiewicz, R. Blair, C. Moodie, A. Isik, A. Erramuzpe, J. Kent, M. Goncalves, E. DuPre, M. Snyder, H. Oya, S. Ghosh, J. Wright, J. Durnez, R. Pol-drack, and K. Gorgolewski, “fmrip: a robust preprocessing pipeline for functional mri,” *Nature Methods*, vol. 16, 01 2019.
- [47] O. Esteban, R. Ciric, K. Finc, R. Blair, C. Markiewicz, C. Moodie, J. Kent, M. Goncalves, E. DuPre, D. Gomez, Z. Ye, T. Salo, R. Valabregue, I. Amlen, F. Liem, N. Jacoby, H. Stojić, M. Cieslak, S. Urchs, and K. Gorgolewski, “Analysis of task-based functional mri data preprocessed with fmrip,” *Nature Protocols*, vol. 15, 06 2020.
- [48] F. Pedregosa, G. Varoquaux, A. Gramfort, V. Michel, B. Thirion, O. Grisel, M. Blondel, P. Prettenhofer, R. Weiss, V. Dubourg, J. Vanderplas, A. Passos, D. Cournapeau, M. Brucher, M. Perrot, and E. Duchesnay, “Scikit-learn: Machine learning in Python,” *Journal of Machine Learning Research*, vol. 12, pp. 2825–2830, 2011.
- [49] A. Abraham, F. Pedregosa, M. Eickenberg, P. Gervais, A. Mueller, J. Kossaifi, A. Gramfort, B. Thirion, and G. Varoquaux, “Machine learning for neuroimaging with scikit-learn,” *Frontiers in neuroinformatics*, vol. 8, p. 14, 02 2014.
- [50] S. Fang and Q. Zhu, “Independent gaussian distributions minimize the kullback-leibler (kl) divergence from independent gaussian distributions,” *Cornell University - arXiv*, Nov 2020.

- [51] C. Blundell, J. Cornebise, K. Kavukcuoglu, and D. Wierstra, “Weight uncertainty in neural networks,” *arXiv: Machine Learning*, May 2015.
- [52] K. Hornik, “Approximation capabilities of multilayer feedforward networks,” *Neural Networks*, vol. 4, no. 2, pp. 251–257, 1991.
- [53] S. Haykin, *Neural Networks: A Comprehensive Foundation, Volume 2*. Prentice Hall, 1998.
- [54] T. Teshima, I. Ishikawa, K. Tojo, K. Oono, M. Ikeda, and M. Sugiyama, “Coupling-based invertible neural networks are universal diffeomorphism approximators,” in *Advances in Neural Information Processing Systems*, vol. 33, 2020, p. 3362–3373.
- [55] T. Teshima, K. Tojo, M. Ikeda, I. Ishikawa, and K. Oono, “Universal approximation property of neural ordinary differential equations,” *arXiv preprint arXiv:2012.02414*, 2017.